

Southern Methodist University

SMU Scholar

---

Mechanical Engineering Research Theses and  
Dissertations

Mechanical Engineering

---

Spring 5-13-2023

## Transport Mechanisms in Electrochemical Immunoassay Biosensors with Applications to SARSCOV-2 Neutralizing Antibody Detection

Mohammad Karim Dehghan Manshadi  
*Southern Methodist University*, [mdehghanmanshadi@smu.edu](mailto:mdehghanmanshadi@smu.edu)

Follow this and additional works at: [https://scholar.smu.edu/engineering\\_mechanical\\_etds](https://scholar.smu.edu/engineering_mechanical_etds)



Part of the [Engineering Commons](#)

---

### Recommended Citation

Dehghan Manshadi, Mohammad Karim, "Transport Mechanisms in Electrochemical Immunoassay Biosensors with Applications to SARSCOV-2 Neutralizing Antibody Detection" (2023). *Mechanical Engineering Research Theses and Dissertations*. 55.

[https://scholar.smu.edu/engineering\\_mechanical\\_etds/55](https://scholar.smu.edu/engineering_mechanical_etds/55)

This Dissertation is brought to you for free and open access by the Mechanical Engineering at SMU Scholar. It has been accepted for inclusion in Mechanical Engineering Research Theses and Dissertations by an authorized administrator of SMU Scholar. For more information, please visit <http://digitalrepository.smu.edu>.

TRANSPORT MECHANISMS IN ELECTROCHEMICAL IMMUNOASSAY BIOSENSORS  
WITH APPLICATIONS TO SARS-COV-2 NEUTRALIZING ANTIBODY DETECTION

Approved by:

---

Prof. Ali Beskok  
Professor of Mechanical Engineering

---

Prof. Paul S. Krueger  
Professor of Mechanical Engineering

---

Prof. Peter Raad  
Professor of Mechanical Engineering

---

Prof. David Willis  
Associate Professor of Mechanical Engineering

---

Prof. Jung-Chih Chiao  
Professor of Electrical Engineering

Transport Mechanisms in Electrochemical Immunoassay Biosensors with Applications to SARS-  
COV-2 Neutralizing Antibody Detection

A Dissertation Presented to the Graduate Faculty of  
Lyle School of Engineering  
Southern Methodist University

in

Partial Fulfillment of the Requirements

for the degree of

Doctor of Philosophy

with a

Major in Mechanical Engineering

by

Mohammad Karim Dehghan Manshadi

(B.Sc., Mechanical Engineering, Shiraz University, Iran, 2012)  
(M.Sc., Mechanical Engineering, Shiraz University, Iran, 2014)

May 13, 2023

Copyright (2023)

Mohammad Karim Dehghan Manshadi

All Rights Reserved

## Acknowledgments

I am deeply grateful to my esteemed thesis advisor, Professor Ali Beskok, for his invaluable guidance, unwavering support, and generous provision of resources and opportunities that have made this research possible. His visionary insights, critical feedback, and constructive criticisms have been instrumental in shaping the direction and focus of this thesis.

I extend my heartfelt appreciation to my thesis committee members, Prof. Paul S. Krueger, Prof. Peter Raad, Prof. David Willis, and Prof. Jung-Chih Chiao, for their valuable feedback, insightful suggestions, and critical assessment of my work, which have significantly enhanced the quality of this thesis.

I am also indebted to my loving wife, Mahsa, and my parents, who have always believed in me and pushed me to be my best; thank you for everything.

Finally, I would like to express my sincere gratitude to my friends who have supported me in various ways throughout my research.

Thank you all for your support and encouragement.

Dehghan Manshadi, Mohammad Karim

B.Sc., Shiraz University, Iran, 2012  
M.Sc., Shiraz University, Iran, 2014

Transport Mechanisms in Electrochemical Immunoassay Biosensors with Applications to SARS-CoV-2 Neutralizing Antibody Detection

Advisor: Professor Ali Beskok

Doctor of Philosophy conferred May 13, 2023

Dissertation completed April 27, 2023

Biosensors are used in diverse applications spanning from clinical diagnosis and drug discovery to environmental and safety monitoring. Among different types of biosensors, electrochemical ones have demonstrated high sensitivity, short detection time, and selectivity with a low cost, and have been widely used to detect various diseases.

In this thesis, we have introduced an inexpensive, rapid, sensitive, and quantifiable impedance-based immunosensors to evaluate SARS-CoV-2 neutralizing antibody (NAb), which shows the real protective immunity against COVID-19. We demonstrated that our device enabled assessment of NAb in a physiological buffer with conductivity equivalent to that of blood plasma. This technique can be used to evaluate NAb in people's blood serum from 50 ng/ml to 190 ng/ml before receiving further COVID vaccine doses. We further analyzed Joule heating induced transport phenomena as a potential method to increase detection in electrochemical biosensors. Buoyancy-driven and AC electrothermal (ACET) flows are the main transport mechanisms that induce two competing flows. Using a scaling analysis, we introduced a new non-dimensional parameter, which enabled the construction of a phase-diagram that can predict the dominance of ACET and buoyancy driven flows as functions of the channel size and electric field.

Table of Contents

Acknowledgments..... iv

CHAPTER 1: INTRODUCTION.....1

CHAPTER 2: THEORY .....8

    2.1. ACEK scaling analysis .....8

    2.2. Joule heating based transport theory .....11

CHAPTER 3: AN IMPEDANCE-BASED NEUTRALIZING ANTIBODY DETECTION  
BIOSENSOR WITH APPLICATION TO SARS-COV-2 INFECTION .....16

    3.1. Materials and Methods.....17

        3.1.1. Detection mechanism.....17

        3.1.2. Numerical simulation.....18

        3.1.3. Bovine antibody and antigen detection procedure.....19

        3.1.4. Sensor specificity and selectivity test .....21

        3.1.5. SARS-CoV-2 Nab detection procedure .....22

    3.2. Results and Discussion .....23

    3.3. Conclusion .....33

CHAPTER 4: COMPETING EFFECTS OF BUOYANCY-DRIVEN AND  
ELECTROTHERMAL FLOWS FOR JOULE HEATING-INDUCED TRANSPORT IN  
MICROCHANNELS .....35

    4.1. Materials and Methods.....36

        4.1.1. Numerical simulation.....36

        4.1.2. Device fabrication and experimental setup.....38

4.1.3. Particle image velocimetry (PIV) .....	40
4.2. Results and Discussion .....	42
4.3. Conclusion .....	60
CHAPTER 5: EFFECT OF GOLD NANOSTRUCTURED ELECTRODES ON BIOSENSING EFFICIENCY.....	62
5.1. Materials and method.....	63
5.1.1. Device fabrication and experimental setup.....	63
5.1.2. Buffer preparation and immobilization procedure.....	65
5.2. Results and discussions.....	67
5.3. Conclusion .....	71
CHAPTER 6: SUMMARY AND FUTURE RESEARCH .....	73
6.1 Summary of the current work .....	73
6.2 Future Research .....	75

## List of Figures

- Figure 3.1.** SAW resonator: **A)** size and **B)** modified chip with the interdigitated electrodes. **C)** Schematic of experimental setup and the detection mechanism. .... 21
- Figure 3.2.** The schematic detection mechanism for the SARS-CoV-2 specific NAbs... 23
- Figure 3.3.** Voltage and antibody immobilization effects on **A)** impedance magnitude and **B)** phase angle of the chip impedance. **C)** Impedance magnitudes before ( $t=0$ ) and after ( $t=120$  s) antibody-antigen interaction at different PBS concentrations. **D)** Impedance magnitude changes before and after antibody-antigen interaction in the frequency range from 100 Hz to 10 MHz for different PBS dilutions. .... 24
- Figure 3.4.** Detection of different antigen concentrations in **A)** 0.01xPBS buffer, **B)** 0.1xPBS buffer, and **C)** 1xPBS buffer. **D)** Standard deviation of LOD for each PBS buffer. All data for 0.01xPBS and 0.1xPBS were obtained at 100 mV and 100 Hz. For 1xPBS, the data was obtained at 100 mV and 600 Hz..... 27
- Figure 3.5.** Detection of different antigen concentrations in **A)** IgG-free BSA and **B)** Mouse serum (MS) to study specificity and selectivity of detection, respectively. All data were obtained for 0.1xPBS at 100 mV and 100 Hz..... 28
- Figure 3.6.** Concentration results from simulations. **A)** Contour plot of the normalized anti-bovine IgG concentration ( $[AB]/[A_0]$ ) at the initial time ( $t=0$ ) and ( $t=120$  s). **B)** Normalized concentration of the interacted anti-bovine IgG-bovine IgG ( $[AB]/[A_0]$ ) on the surface of the electrodes. .... 30
- Figure 3.7.** ACE2 immobilization effects on **A)** impedance magnitude and **B)** the phase angle of the chip impedance. **C)** LOD for RBD-hACE2 interaction for different NAbs concentrations. **D)** The NAb concentration and impedance change relationship for the device. All data were obtained using 0.1xPBS buffer for dilution at 100 mV and 100 Hz. .... 31
- Figure 4.1.** **A)** the triangular grid produced by COMSOL in the computational domain. **B)** Maximum velocity magnitude induced in the fluid when  $H=300 \mu\text{m}$ ,  $\sigma=1.2 \text{ S/m}$ , and  $\phi=7 V_{pp}$  for different number of grids. Speed contours, velocity vectors and the streamlines in the domain with **C)** 17864, **D)** 156592, **E)** 969660, **F)** 2806012 number of elements..... 38
- Figure 4.2.** **A)** Fabricated device using the photolithography method, **B)** Experimental setup. .... 40
- Figure 4.3.** Streamlines, velocity vectors, and the speed contours obtained for Joule heating induced transport in a microchannel with electrodes placed at the bottom (**A)** and top (**B)** of the channel. The gravitational acceleration is downwards. **C)** Streamlines, velocity

vectors, and the speed contours obtained for Joule heating induced transport in a microchannel with electrodes placed at the bottom with upward gravitational acceleration. A portion of the simulation domain is shown, while the used geometry ( $L=100\ \mu\text{m}$  and  $d=50\ \mu\text{m}$ ), applied voltage ( $7\ V_{pp}$ ), and the ionic conductivity of the fluid ( $\sigma=1.2\ \text{S/m}$ ) were matched with the values reported in [31]. **D)** Simulation results compared with the experimental data in [16] and previously used model, **E)** A schematic view of the simulated and fabricated device. .... 43

**Figure 4.4.** The phase-diagram for dominance of  $F_e$  versus  $F_b$  in the microchannel is based on their induced velocity ratio. This ratio was found for channel heights ( $H$ ) varying from  $10\ \mu\text{m}$  to  $1\ \text{mm}$  and applied electric potentials ( $\phi$ ) varying from  $0.3\ V_{pp}$  to  $10\ V_{pp}$ . The minimum velocity ( $1\ \mu\text{m/s}$ ) line for three different buffer conductivities of  $\sigma = 1.2\ \text{S/m}$ ,  $\sigma = 0.6\ \text{S/m}$ , and  $\sigma = 0.24\ \text{S/m}$  are also shown. .... 50

**Figure 4.5.** Streamlines, velocity vectors, and the speed contours in a  $300\ \mu\text{m}$  height channel under the effects of  $F_e$ ,  $F_b$ , or  $F_e+F_b$  at **A)**  $\phi=1\ V_{pp}$  and **B)**  $\phi=7\ V_{pp}$  electric potential..... 52

**Figure 4.6.** Velocity vectors, speed contours and the streamlines for **A)**  $\phi=1\ V_{pp}$ ,  $\sigma=1.2\ \text{S/m}$ , **B)**  $\phi=1\ V_{pp}$ ,  $\sigma=0.24\ \text{S/m}$ , **C)**  $\phi=7\ V_{pp}$ ,  $\sigma=1.2\ \text{S/m}$ , **D)**  $\phi=7\ V_{pp}$ ,  $\sigma=0.24\ \text{S/m}$ . **E)** Maximum induced temperature in the channel for three different buffer conductivities. **F)** Maximum induced velocity in the channel for three different buffer conductivities. .... 54

**Figure 4.7.** Effects of  $H$  and  $\phi_0$  on the streamlines, velocity vectors and speed contours. Column A shows the effects of increasing applied potential at constant channel height  $H=300\ \mu\text{m}$ . Column B shows the effects of increasing channel height at constant applied electric potential of  $\phi=7\ V_{pp}$ . .... 55

**Figure 4.8.** Velocity vectors, speed contours and the streamlines at  $\phi=7\ V_{pp}$  and for different channel heights of **A)**  $H=50\ \mu\text{m}$ , **B)**  $H=100\ \mu\text{m}$ , **C)**  $H=200\ \mu\text{m}$ , **D)**  $H=300\ \mu\text{m}$ , **E)**  $H=500\ \mu\text{m}$ , **F)**  $H=800\ \mu\text{m}$ . .... 56

**Figure 4.9.** Temperature contours around the pair of electrodes within a microchannel with different heights for **A)** conduction only, and **B)** a combination of conduction and convection heat transfer mechanisms. The Rayleigh numbers are 182, 1200, 2850, and 5560 for column B, i to iv, respectively. The applied electric potential is  $\phi=7\ V_{pp}$ . .... 58

**Figure 4.10.** Experimental results for flow field at an ROI  $70\ \mu\text{m}$  above the electrodes. **A)** PIV result for the velocity field in the ROI at  $\phi_0=7\ V_{pp}$  from the bottom view of the electrodes, **B)** Velocity magnitude in the y-direction compared with the simulation result at  $\phi_0=7\ V_{pp}$ , **C)** Average velocity magnitudes in the ROI compared with the numerical simulation results at different applied voltages. .... 60

**Figure 5.1.** **A)** Fabricated device using the photolithography method and the gold nanostructure on the electrode surface, **B)** Experimental setup..... 65

<b>Figure 5.2.</b> Comparing <b>A)</b> impedance magnitude and <b>B)</b> phase angle for GPE and GNE .....	68
<b>Figure 5.3.</b> Impedance spectra of the electrodes in 1xPBS, for electrodes with 100 ng/ml antigen immobilized on the electrode surface, and 30 min after antibody-antigen interactions. <b>A)</b> GPE Impedance magnitudes, <b>B)</b> GPE phase angle, <b>C)</b> GNE Impedance magnitudes, <b>D)</b> GNE phase angle.....	69
<b>Figure 5.4.</b> Impedance changes 30 minutes after antibody-antigen interaction for 100 ng/ml antigen concentrations diluted in 1xPBS applied on the immobilized electrode surface for <b>A)</b> GPE and <b>B)</b> GNE.....	70
<b>Figure 5.5.</b> Comparing $\Delta Z / Z_0 $ for GPE and GNE .....	71

## List of Tables

<b>Table 3.1.</b> Reagent displacement in the device due to the ACEO, ACET, DEP, and Brownian motion in 1 (s).....	29
<b>Table 4.1.</b> Characteristic parameters used for non-dimensionalization of the steady Stokes and energy equations.....	46

## Chapter 1

### INTRODUCTION

Coronavirus disease-2019 (COVID-19) is an unprecedented pandemic. COVID-19 originated from severe acute respiratory syndrome coronavirus 2 (SARS-CoV-2). The first step of SARS-CoV-2 entry into host cells is the binding of the spike (S) protein via receptor-binding domain (RBD) to angiotensin-converting enzyme 2 (ACE2) and subsequent membrane fusion [1]. After SARS-CoV-2 infection or vaccination, serum-neutralizing antibodies (NAbs) rapidly appear to inactivate the viral RBDs [2]. However, the concentrations of NAbs obtained by current vaccines have been shown to vary by as much as 25 fold after several months [3]. The individualized evaluation of the neutralizing capacity of anti-SARS-CoV-2 antibodies is important because it can provide insights into real protective immunity. However, continuous testing of a large population requires the development of accurate, fast, quantifiable, and inexpensive biosensors based on detecting human antibodies.

While antibody and antigen detections with lateral flow assays are available [4], which are quick, affordable, and accessible without tedious sample processing logistics issues, they do not provide quantitative values to assess antibodies; rather, they simply show a positive or negative result. Currently, the lateral flow technology is not capable of neutralizing antibody assessment either. Standard virus plaque reduction neutralization test assays used to evaluate NAbs in blocking live infectious SARS-CoV-2 virus require their operation in high biosafety rating laboratories [5]. The procedures are time-consuming, expensive, and require skilled operators. GenScript's cPass neutralization antibody assay has received

Emergency Use Authorization (EUA) by U.S. Food and Drug Administration (FDA) [6]. However, the detection kit provides semi-quantitative evaluation and requires skills to operate. Several methods have been proposed to pursue affordable and convenient point-of-care NAb detection methods. A vertical-flow cellulose paper-based assay showed comparable detection results to lab-based ones [7]. The method measures the interaction between RBD and ACE2 receptors, and the high-affinity signals specific to NAb enable fast evaluation without the requirement of live viruses. A workflow for cellulose pull-down virus neutralization tests (cpVNT) and optical image acquisition for colorimetric signal processing are needed for further process refinement, automation, and electronics integration for the vertical flow assays [7-9]. In comparison, electrochemical sensors also show great promise as they provide high sensitivity, shorter detection time, accurate selectivity, and lower costs [10].

In electrochemical sensors, electrodes are the main part where biomolecules (e.g., enzyme [11], antibody [12], and nucleic acid [13]) are immobilized via different approaches [14]. Then, antigen-antibody interactions (affinity biosensors) on the electrode surface are transduced to electrical signals (e.g., impedance, current, voltage, etc.) [15]. Detection in affinity biosensors is based on specific binding between determined reagents (e.g., a receptor, nucleic acid, or an antibody). Therefore, the interaction of the biological component and the analyte is crucial to achieving detection [16]. The capacitive sensing method is one of the introduced alternating current electrokinetic (ACEK) based immunosensors [17]. Applying AC electric potentials in ionized media induces diffuse charge at the electrode/electrolyte interface or electric double layer (EDL). Molecular binding is characterized by changes in the EDL's electrical signal (capacitance change rate).

Capacitive sensing allows real-time measurements of fast binding processes [17, 18] and has been used for various applications [18-21]. Alternating current electrokinetic (ACEK) transport phenomena, including AC Electroosmosis (ACEO), AC Electrothermal (ACET), and Dielectrophoresis (DEP), are widely reported to enhance detection in affinity biosensors in the references. However, there are no detailed investigations to prove these claims.

It is important to understand the relative effects of ACEO, ACET, and DEP forces on the sensor performance. For example, the suspended particles can experience negative DEP at certain frequencies depending on the ionic conductivity, which will repel/attract them from the electrode surfaces [22]. Also, the ACET flow is induced by variations of fluid permittivity and conductivity under Joule heating [23]. Therefore, applying high electric potentials can create large temperature variations that can denature proteins on the sensor surface, while increased ACET fluid velocities can lead to large shear stresses on the sensor surfaces, and mild ACET flows can enhance mixing and enable convection for fast measurements. ACET flows have been widely reported in electrochemical immunoassay biosensors to enhance detection [18, 21, 24-26]. This is because most biological microfluidic applications utilize physiological buffers with large conductivities ( $\sigma \approx 1.5$  S/m), where the Joule heating is significant. An interesting transport phenomenon due to Joule heating is the electrothermal flow (ETF) that happens due to the temperature dependence of the buffer permittivity and conductivity. It is essential to indicate that nonuniform heating of the fluid due to Joule heating also results in buoyancy driven flows (BDF), where the low density hot-fluid rises, and the high density cold-fluid falls under the gravitational body force. Since the BDF co-occurs with ETF, the importance of these two

phenomena needs to be characterized for their proper use in microfluidic applications. Most previous theoretical and numerical investigations in the literature considered ACET flow without the buoyancy driven flow [27, 28]. However, these two effects may enhance or impede each other while inducing unique local flow patterns in microfluidic systems.

Loire et al. [29] investigated the importance of electrothermal and buoyancy driven flows numerically and experimentally. Their numerical model solved the coupled electric field, fluid flow, and heat transfer equations with temperature dependent fluid properties. They numerically compared the velocity fields around a pair of electrodes obtained with or without the buoyancy effects. The numerical simulation results were also compared with the velocity measurements using the micro-particle-image-velocimetry ( $\mu$ -PIV) technique. Numerical results matched the experiments when the buoyancy effects were considered. In a following study, William [30] used the numerical model developed by Loire et al. [29], demonstrating that buoyancy driven flow induced by a thin film heater could considerably increase the flowrate in an ETF pump, proving the importance of BDF in such microfluidic systems. Although these investigations proved the importance of considering BDF, an incorrect buoyancy force direction was considered in their simulations.

Lu et al. [31] conducted a series of  $\mu$ -PIV experiments of ACET flow occurring between two parallel electrodes in microchannel heights varying from 800  $\mu\text{m}$  to 300  $\mu\text{m}$ , and measured the velocity fields at the electrode gap region and downstream/upstream regions of the microelectrode. They observed two small vortices in the electrode gap region due to the ACET flow, while two large vortices in reversed directions were identified in the upstream/downstream regions due to the buoyancy driven flow. Lu et al. [31] also presented numerical simulation results that modeled both ACET and BDF with spatially

varying material properties as a function of temperature. Although they reported the co-occurrence of these two types of flows, they did not present a systematic investigation as a function of channel dimensions and operation conditions.

In addition to the Joule-heating based transport to increase detection, Koklu et al. [26] introduced a rapid and sensitive biosensor by incorporating the structural advantage of nanorod-covered interdigitated electrodes and the induced ACET around the electrodes in high conductive buffers. They demonstrated that the limit of detection of the planar sensor increased almost 1.6 times more by using the nanorod structured electrodes, which increased the surface area of the active binding regions. The fundamental limitation of the usage of planar surface electrodes is the electrode polarization (EP) effect. The EP effect usually occurs at the sub-MHz frequency range in high-conductive media. It stems from ions accumulation at the electrode/electrolyte interface, which creates a large interfacial capacitance and electric potential drop. Therefore, electrode sensitivity and measurement accuracy are reduced. To avoid the EP effect, Koklu et al. [26] suggested a 5 (MHz) detection frequency which is far away from EP frequency range.

In this thesis, first, an interdigitated electrode was modified as a biosensor to characterize SARS-CoV-2 NAbs. The interaction between bovine IgG and anti-bovine IgG characterized the sensor's detection potential. A wide range of frequencies varying from 100 Hz to 10 MHz and different voltage magnitudes were considered to find the optimum detection frequency and voltage. The impedance spectroscopy technique was chosen to record the impedance of the tested devices in real time during antibody-antigen interaction on the electrode surface. Then, a scaling analysis was used to find the order of magnitude of the ACEK forces, including ACEO, ACET, and DEP, in three different PBS buffer

dilutions (0.01xPBS, 0.1xPBS, and 1xPBS). The orders of magnitude of antibody displacement due to these forces were compared with the Brownian motion of the IgGs, which is the basis for mass diffusion. A numerical simulation technique was utilized to demonstrate the validity of the theoretical analysis. Then, the device was employed for SARS-CoV-2 NAbs detection. When a person gets affected by SARS-CoV-2, viral RBDs attach to the human ACE2 (hACE2) and enter the host cell through membrane fusion. Viral RBDs are neutralized by NAbs and thus deactivated. The NAbs concentration in the blood serum determines immunity strength after vaccination. To evaluate this concentration using the proposed device, the electrode surface was immobilized with human ACE2 (hACE2), reacting to the viral RBD. Then, the RBD buffers with different NAb concentrations were applied to the device, and the resultant electrical signals were recorded.

Then, we studied the relative importance of the buoyancy-driven, and ACET flows that simultaneously occur due to Joule heating in high conductivity buffers. We first present proper nondimensionalization of the energy and momentum equations and then identify the ratio of the electrothermal and buoyancy-driven flow velocities as a *new non-dimensional parameter* to determine the dominant regions of each flow within a *phase-diagram*. Using the flow generated by a symmetric pair of planar electrodes in a microchannel as a characteristic system, we present numerical results of mixed ACET and buoyancy driven flows for varying channel dimensions, applied electric fields and ionic conductivities, and verify the phase-diagram. This is followed by the  $\mu$ -PIV measurements of the resulting flow to validate the numerical results.

Finally, we studied the electrodeposition technique in order to enlarge the electrode/electrolyte area, which results in active binding sites on the electrode as well as reducing EP effect. Using our experiences in developing immunoassay biosensors and reducing EP effect, an interdigitated electrode pair with electrodeposited gold nanostructures is used to characterize the reaction between bovine IgG and anti-bovine IgG in the high conductive buffer. The detection response was indicated by recording the impedance of the devices during antibody–antigen interaction on the electrode surface. In order to find the optimum detection frequency of the sensor, the impedance of the microfluidics device was measured in a range of frequencies varying from 100 Hz to 10 MHz.

## Chapter 2

### THEORY

In this section, the ACEK scaling analysis and Joule heating based transport phenomenon equations are explained.

#### 2.1. ACEK scaling analysis

In previous studies, ACEK phenomena have been suggested to enhance detection by increasing mixing time. ACEO, ACET, and DEP are the main ACEK phenomena that induce forces on the antibodies and bring them to the detection region [17-19]. It is important to understand the relative effects of ACEO, ACET, and DEP forces on the sensor performance. For example, the suspended particles can experience negative DEP at certain frequencies depending on the ionic conductivity, which will repel them from the electrode surfaces [22]. Also, the ACET flow is induced by variations of fluid permittivity and conductivity under Joule heating [23]. Therefore, applying high electric potentials can create large temperature variations that can denature proteins on the sensor surface, while increased ACET fluid velocities can lead to large shear stresses on the sensor surfaces. However, positive DEP will enhance detection by attracting proteins and particles onto the sensor surfaces, and mild ACET flows can enhance mixing and enable convection for fast measurements. Here we consider the relative magnitudes of the resultant displacement due to these forces during detection using several theoretical models. The magnitudes of these displacements are compared with the displacement due to Brownian motion. These models

are used to determine the dominance of each phenomenon for different PBS dilutions. Details for these models are provided in the literature [23, 32, 33]. The ACEO flow is generated in low conductivity fluid due to the electric field effects on induced diffuse charges near the electrode surface or EDL. The specimen displacement in the buffer due to the ACEO flow from scaling analysis is [32]:

$$X_{ACEO} = \Lambda \frac{\varepsilon V^2}{8\eta r} \frac{\Omega^2}{(1 + \Omega^2)^2} t \quad (2.1)$$

where  $\varepsilon$  is the solution permittivity ( $7.083 \times 10^{-10}$  F/m),  $\eta$  is the dynamic viscosity of the solution (0.001 Pa·s),  $r$  is the half of the electrode spacing (1  $\mu$ m),  $V$  is the applied voltage,  $\Lambda$  defined as  $C_s/(C_s+C_D)$ , where  $C_s$  is the capacitance of the Stern layer (0.007 F/m<sup>2</sup>) [33],  $C_D=\varepsilon/\lambda_D$  is the capacitance of the diffuse layer, and  $\Omega$  is equal to  $\Lambda\omega\pi r/2\sigma\lambda_D$ , where  $\omega$  is the radian frequency ( $2\pi f$ ),  $t$  is time,  $\sigma$  is the conductivity of the fluid as 0.016 (S/m), 0.16 (S/m), 1.6 (S/m) for 0.01xPBS, 0.1xPBS, 1xPBS, respectively, and  $\lambda_D$  is the Debye length which is 0.7 (nm), 2.4 (nm), 7.4 (nm) for 1xPBS, 0.1xPBS, 0.01xPBS, respectively [34].

ACET arises from Joule heating due to the electric current passing through the buffer increasing with increased ionic conductivity and inducing ACET flow in the fluid due to the temperature dependencies of the electrical permittivity and conductivity of the medium [35, 36]. The ACET displacement of the particle is also found from scaling analysis as [23]:

$$X_{ACET} = \frac{1}{192\pi^2} \frac{M}{T} \frac{\varepsilon\sigma V^4}{k\eta L_c} t \quad (2.2)$$

where  $T$  is the temperature (293.15 K),  $k$  is the thermal conductivity (0.6 W/m·K),  $L_c$  is the characteristic length for electrothermal flow, which is equal to the typical dimension of the chip, and  $M$  is the electrothermal factor defined as:

$$M = \frac{(C_\sigma - C_\varepsilon)T}{1 + (\omega\varepsilon/\sigma)^2} + \frac{1}{2}C_\varepsilon T \quad (2.3)$$

In this equation,  $C_\sigma = \frac{1}{\sigma(T_0)} \frac{\partial \sigma}{\partial T} |_{T_0} \approx 0.02 K^{-1}$  and  $C_\varepsilon = \frac{1}{\varepsilon(T_0)} \frac{\partial \varepsilon}{\partial T} |_{T_0} \approx -0.004 K^{-1}$ .

A dielectrophoretic (DEP) force is imposed on the suspended particles based on their relative polarizability with respect to the ionic fluid [37]. At a given AC frequency, more polarizable particles than the fluid are attracted to the high electric field regions near the electrodes, exhibiting positive DEP [38]. Otherwise, they are repelled from the near electrode regions (i.e., negative DEP). The induced displacement on the particles due to the DEP force can be found as [32]:

$$X_{DEP} = \frac{1}{3\pi^2} Re\{K\} \frac{a^2 \varepsilon \beta^2 V_0^2}{\eta r^3} t \quad (2.4)$$

where  $a$  is the particle radius ( $2a=10$  nm [34]),  $\beta$  is  $\Omega^2/(1+\Omega^2)$ ,  $K = \left[ \frac{\varepsilon_p^* - \varepsilon_m^*}{\varepsilon_p^* + 2\varepsilon_m^*} \right]$  is the Clausius-Mossotti (CM) factor,  $\varepsilon_p^*$  and  $\varepsilon_m^*$  are the complex permittivities of particle and medium, respectively. Complex permittivity is  $\varepsilon^* = \varepsilon - j\left(\frac{\sigma}{\omega\varepsilon}\right)$  with  $\varepsilon_p=3.54168 \times 10^{-11}$  F/m,  $\sigma_p=0.22$  S/m [39, 40].

The displacement of particles due to the Brownian motion can be found in [33]:

$$X_{Brownian} = \left( \frac{k_B T}{3\pi a \eta} t \right)^{1/2} \quad (2.5)$$

where  $k_B$  is Boltzmann constant ( $1.38E-23$  (m<sup>2</sup>·kg/s<sup>2</sup>·K)) and  $T$  is temperature in °K.

In chapter 3, the above equations are used to determine the order of magnitudes for reagent displacement in the sensor for different buffer conductivities.

## 2.2. Joule heating based transport theory

Electrokinetic transport refers to the fluid and particle motion due to an externally applied electric field. AC electrothermal flow (ETF) arises from the nonuniform permittivity and conductivity of the fluid due to the temperature gradient in the domain, typically induced by Joule heating. Numerical modeling of this flow requires a solution for the electric field equations coupled with the fluid flow and energy equations. The electric field is determined by Gauss' law, charge conservation, and Faraday's law, given as follows:

$$\nabla \cdot (\varepsilon \nabla \varphi) = \rho_e \quad (2.6)$$

$$\frac{\partial \rho_e}{\partial t} + \nabla \cdot (\sigma \nabla \varphi) = 0 \quad (2.7)$$

$$\nabla \times \nabla \varphi = 0 \quad (2.8)$$

where  $\varepsilon$  (F/m) is the electrical permittivity,  $\rho_e$  (C/m<sup>3</sup>) is the space charge density,  $\sigma$  (S/m) is the electrical conductivity,  $t$  (s) is time, and  $\varphi$  (V) is the electric potential. Considering small variations in permittivity and conductivity with temperature, quasi-static electric potential ( $\varphi$ ) can be calculated by

$$\nabla^2 \varphi = 0 \quad (2.9)$$

The resultant electric field  $\mathbf{E}$  (V/m) is defined as the gradient of the electric potential ( $\mathbf{E} = -\nabla \varphi$ ). In order to solve this equation,  $\pm \varphi$  (V) is applied on the electrodes, while zero charge condition is applied on the rest of the boundaries.

The electric field applied in high conductivity medium generates Joule heating that induces temperature gradients in the microchannel. Therefore, the energy equation is solved with the Joule heating source term.

$$\rho_m C_p \left( \frac{\partial T}{\partial t} + (\mathbf{u} \cdot \nabla) T \right) = \nabla \cdot (k_m \nabla T) + S \quad (2.10)$$

$$S = \sigma (\mathbf{E} \cdot \mathbf{E}) \quad (2.11)$$

where  $\rho_m$  (kg/m<sup>3</sup>) is the fluid density,  $C_p$  (J/K) is the heat capacitance,  $T$  (K) is temperature,  $u$  (m/s) is velocity,  $k_m$  (W/m.K) is the fluid heat conductivity, and  $S$  (J/m<sup>3</sup>) is the Joule heating source term.

After applying the electric field, the temperature field rapidly reaches a stationary state with both time-independent and oscillating components. The effect of the oscillating component on fluid dynamics is negligible for AC electric field frequencies higher than 1 kHz [33]. For microfluidic devices, the convective term in **Equation 2.10** is insignificant, and the time to reach a steady state for heat transfer ( $t = \frac{\rho_0 C_p L_c^2}{k_m}$ , where  $L_c$  is the characteristic length) is often smaller than 0.1s. Based on these simplifications, the energy equation reduces to the following form with a time-averaged source term,

$$\nabla \cdot (k_m \nabla T) + \langle S \rangle = 0 \quad (2.12)$$

$$\langle S \rangle = \frac{1}{2} \sigma (\mathbf{E} \cdot \mathbf{E}) \quad (2.13)$$

where the 1/2 coefficient in front of (**Equation 2.13**) comes from assuming  $\pm \varphi$  (V) applied potential on the electrodes.

Since the channel is surrounded by a solid glass domain, heat generated in the fluid transfers through the walls to the environment. Temperature distribution in the solid section is determined from the steady state heat conduction equation as follows:

$$\nabla \cdot (k_s \nabla T) = 0 \quad (2.14)$$

where the  $k_s$  (W/m.K) is the solid's heat conductivity. Heat transfer across the fluid-solid interface is determined by considering the temperature gradients with heat transfer coefficients at the interface. Simulation software uses the material properties of both the solid and fluid domains to solve the equations and determine heat transfer across the interface. Since most of the microfluidic devices work at room temperature, a constant temperature (293.15 K) boundary condition was assumed around the solid domain exposed to the surrounding air.

The electric field and temperature gradient in the domain induce electrical and buoyancy forces on the fluid. The resulting flow is determined by the solution of the Navier-Stokes (NS) equation

$$\rho_m \left( \frac{\partial \mathbf{u}}{\partial t} + (\mathbf{u} \cdot \nabla) \mathbf{u} \right) = -\nabla p + \mu \nabla^2 \mathbf{u} + \mathbf{F}_e + \mathbf{F}_b \quad (2.15)$$

where  $\mu$  (Pa.s) is the fluid viscosity,  $p$  (Pa) is the pressure,  $\mathbf{F}_e$  is the electrical force, and  $\mathbf{F}_b$  is the buoyancy force. It is essential to indicate that the fluid density ( $\rho_m$ ), viscosity ( $\mu$ ), and thermal conductivity ( $k_m$ ) are functions of the local temperature, while incompressible flow requires a divergence free velocity field to satisfy the mass conservation.

Microfluidic devices have small characteristic dimensions with low fluid velocities, which often result in the Stokes flow limit, where the Reynolds number,  $Re \ll 1$ . Diffusion time-

scale ( $t = \frac{\rho_m L_c^2}{\mu}$ ) dominates over the convective effects, and fluid flows in these systems reach a steady-state usually less than 0.01 s. Under such simplifications, the steady-state momentum equation becomes

$$-\nabla P + \mu \nabla^2 \mathbf{u} + \mathbf{F}_e + \mathbf{F}_b = \mathbf{0} \quad (2.16)$$

In this equation, the  $\mathbf{F}_e$  and  $\mathbf{F}_b$  are given by

$$\mathbf{F}_e = \frac{1}{2} \cdot \frac{\varepsilon(c_\varepsilon - c_\sigma)}{1 + \left(\frac{2\pi f \varepsilon}{\sigma}\right)^2} (\nabla T \cdot \mathbf{E}) \mathbf{E} - \frac{1}{4} \cdot \varepsilon c_\varepsilon \nabla T (\mathbf{E} \cdot \mathbf{E}) \quad (2.17)$$

$$\mathbf{F}_b = \rho_m \mathbf{g} \quad (2.18)$$

where  $\mathbf{g}$  (m/s<sup>2</sup>) is the gravitational acceleration and  $f$  is the AC electric field frequency.

The parameters  $c_\varepsilon$  and  $c_\sigma$  are obtained from the Taylor series expansion of  $\sigma$  (T) and  $\varepsilon$  (T).

For water,  $c_\varepsilon = \frac{1}{\varepsilon} \frac{\partial \varepsilon}{\partial T} \sim -0.004 \text{ K}^{-1}$ ,  $c_\sigma = \frac{1}{\sigma} \frac{\partial \sigma}{\partial T} \sim 0.02 \text{ K}^{-1}$  at a reference temperature of 298.15 K [41].

The Boussinesq approximation is assumed to model the buoyancy force due to the non-isothermal flow. In microfluidic devices, changes in density due to pressure variations are negligible because of the microscale dimensions (there is no significant change in hydrostatic pressure) [42]. Therefore, the density variation is mainly a function of temperature [43]. Using Taylor series expansion, the fluid density can be written as:

$$\rho_m \cong \rho_0 + \left(\frac{\partial \rho}{\partial T}\right)_p (T - T_0) \quad (2.19)$$

where  $T_0$  is the reference temperature (298.15 K) and  $\rho_0 = \rho_m(T_0)$ . Using the volume expansion coefficient  $\beta = -\frac{1}{\rho_0} \left(\frac{\partial \rho}{\partial T}\right)_p$  [44], this equation is simplified to

$$\rho_m \cong \rho_0 - \rho_0\beta(T - T_0) \quad (2.20)$$

Substitution of this buoyancy force into the steady Stokes equation gives

$$-\nabla p + \mu\nabla^2\mathbf{u} + \mathbf{F}_e + \rho_0\mathbf{g} - \rho_0\beta(T - T_0)\mathbf{g} = \mathbf{0} \quad (2.21)$$

In general, the  $\rho_0\mathbf{g}$  term creates hydrostatic pressure in the system, which can be included in the pressure gradient term. However, the hydrostatic pressure variations in microchannels are negligible due to their minuscule height, so the above equation can be further simplified to:

$$-\nabla(p) + \mu\nabla^2\mathbf{u} + \mathbf{F}_e - \rho_0\beta(T - T_0)\mathbf{g} = \mathbf{0} \quad (2.22)$$

Since this equation is solved in a closed chamber, the atmospheric pressure point constraint is defined as a boundary condition to solve the fluid velocity and pressure distribution. No slip boundary condition is used at all fluid-solid interfaces.

## Chapter 3

### AN IMPEDANCE-BASED NEUTRALIZING ANTIBODY DETECTION BIOSENSOR WITH APPLICATION TO SARS-COV-2 INFECTION

Although safe and efficacious coronavirus disease-2019 (COVID-19) vaccines are available, real protective immunity is revealed by the serum COVID-19 neutralizing antibody (NAb) concentration. Neutralizing antibodies deactivate the virus by attaching to the viral receptor-binding domain (RBD), which interacts with angiotensin-converting enzyme 2 (ACE2) on the human cell. This chapter introduces inexpensive, rapid, sensitive, and quantifiable impedance-based immunosensors to evaluate the NAb. Sensor limit of detection (LOD) is experimentally determined in different buffer dilutions using bovine IgG-anti-bovine IgG interaction. The dominance of AC electrokinetic transport and molecular diffusion in the sensor is investigated using scaling analysis and numerical simulations. The results demonstrated that the sensor detection mechanism is mainly based on the diffusion of the biomolecules onto the electrode surface. After evaluating the sensor working principles, viral RBDs buffers, including different NAb concentrations, are applied to the sensor, immobilized with the human ACE2 (hACE2). Results demonstrate the sensor is capable of NAb detection in the analytical measuring interval (AMI) between 45 (ng/ml) to 185 (ng/ml). Since the present sensor provides fast test results with lower costs, it can be used to assess NAb in people's blood serum before receiving further COVID vaccine doses.

### 3.1. Materials and Methods

#### 3.1.1. Detection mechanism

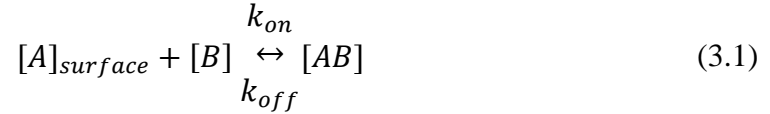
This study utilized the impedance spectroscopy technique to evaluate antibody-antigen binding on the electrode interfaces. The method applies an alternative current (AC) electric field as the stimulus and the corresponding electrical current through the system as the response is measured. Since the applied voltage is frequency dependent, a range of frequencies is applied to obtain comprehensive information from the system to produce an impedance spectrum. Therefore, any change in the impedance spectrum can be interpreted as an electrode/electrolyte interfacial change. Parameters such as electrode potential, temperature, ion concentration, an oxide layer, electrode surface roughness, and impurity adsorption may also result in an interfacial change. However, the sensors were washed and plasma cleaned before any further step, the experiments were performed in temperature controlled environment, and purified buffers were used for dilution purposes. Therefore, the impedance changes were interpreted as molecular bindings. These changes can be described using a simplified equivalent circuit model. EDL and the solution are considered an interfacial capacitor,  $C_{int}$  on the electrodes, and buffer resistance,  $R_s$ , so the device impedance is approximated as  $Z=R_s + 1/j\omega C_{int}$  or  $Z=|Z|e^{i\theta}$ . Molecular bindings increase the dielectric layer on the electrodes and surface topology, which will change the interfacial impedance. Therefore, these changes are considered as the binding events.

### 3.1.2. Numerical simulation

The antibody-antigen interaction on the sensor's electrode surface has also been simulated.

The following equations are considered to model this binding procedure.

The binding of the protein pair is obtained from the following chemical reaction:



where  $[A]_{surface}$  is the target molecule concentration,  $[B]$  is surface receptor concentration, and  $[AB]$  is protein-protein complex concentration. The  $k_{on}$  is the association rate constant ( $2.5E5$  (1/M.s)), and  $k_{off}$  is the dissociation rate constant ( $3E-4$  (1/s)) for the IgG-anti-IgG binding interactions [45]. The surface reaction can be found from the following first-order Langmuir adsorption equation:

$$\frac{\partial[AB]}{\partial t} = k_{on}[A]([B_0] - [AB]) - k_{off}[AB] \quad (3.2)$$

In this equation,  $[B_0]$  is the initial surface concentration of the receptor ( $1.4 \times 10^{-8}$  (mol/m<sup>2</sup>)) [45]. Fick's second law describes the transport of analytes around the surface as follows:

$$\frac{\partial[A]}{\partial t} - D\nabla^2[A] = R \quad (3.3)$$

where  $[A]$  is the bulk concentration of the target molecule and  $D$  is its diffusion coefficient ( $5 \times 10^{-11}$  (m<sup>2</sup>/s)) [45]. The initial concentration of  $[A]$  is assumed to be  $[A_0]$  in the medium.

These equations are solved using the COMSOL Multiphysics.

### 3.1.3. Bovine antibody and antigen detection procedure

1xPBS (~1.6 S/m), 0.1xPBS (~0.16 S/m), and 0.01xPBS (~0.016 S/m) were prepared by 1:10, 1:100, and 1:1000 volume dilution of physiological strength stock solution (10xPBS, Fisher Scientific) with ultrapure deionized (DI) water. To determine the LOD of the present sensor, anti-bovine IgG (H+L) antibody (Jackson ImmunoResearch Laboratories Inc.) binding to bovine IgG whole molecules (Jackson ImmunoResearch Laboratories Inc.) was investigated. The bovine IgG was diluted with proper PBS buffer to 10  $\mu\text{g}/\text{mL}$  for immobilization on the electrode surface. Also, the anti-bovine IgG in PBS with concentrations from 1 ng/ml to 10,000 ng/ml based on the buffer conductivity was used for detection purposes.

A commercially available SAW resonator (RO3101A, Murata Electronics) was modified to employ the interdigitated microelectrode arrays for antibody-antigen binding purposes. This type of resonator has a small electrode size/spacing (2  $\mu\text{m}/2 \mu\text{m}$ ), made of aluminum at a low price, making biosensing more affordable and accurate than other methods like ELISA (**Figure 3.1A**). The modification includes removing the metallic cap on top of the electrodes and connecting two wires (**Figure 3.1B**). Then, the resonator was cleaned thoroughly using acetone, isopropyl alcohol, and DI water for 15 (s) for each. The electrodes are placed inside a 5 mm  $\times$  3.5 mm  $\times$  1.5 mm container, which serves as a microchamber. In previous studies, an increase in the hydrophilicity of the surface using oxygen plasma cleaner was introduced to enhance the immobilization of the protein on the electrode surface [18]. Therefore, the electrode surface for different devices was treated with plasma cleaner (PDC-32G, HARRICK PLASMA) for 30 s. Then, IgG whole molecule

buffer can wet the electrode surface properly. It should be noted that all the tested devices were plasma-treated for 30 s before immobilization.

After plasma treatment, the chamber was filled with bovine IgG whole molecules (10  $\mu\text{g/ml}$ ) diluted with PBS solution. The loaded chip was kept inside a humidity chamber at 4°C for 12 hours to functionalize the electrodes. Afterward, the unbounded IgG on the electrodes was washed away using PBS, and the chip was ready to detect anti-bovine IgG.

To start the detection, the chip wires were connected to an impedance analyzer (HP Agilent 4194A) which applied the desired electric potential in the specified frequency and recorded the impedance simultaneously. **Figure 3.1C** shows the schematic of the experimental setup and the detection mechanism. To assure the accuracy of the applied voltage and frequency by the impedance analyzer, an oscilloscope (TDS 2014B, Tektronix) was used to measure these two parameters before starting the experiments. Then, the chamber was filled with the diluted anti-bovine IgG in desired concentrations, and impedance changes were recorded continuously while the AC voltage was applied to the chip.

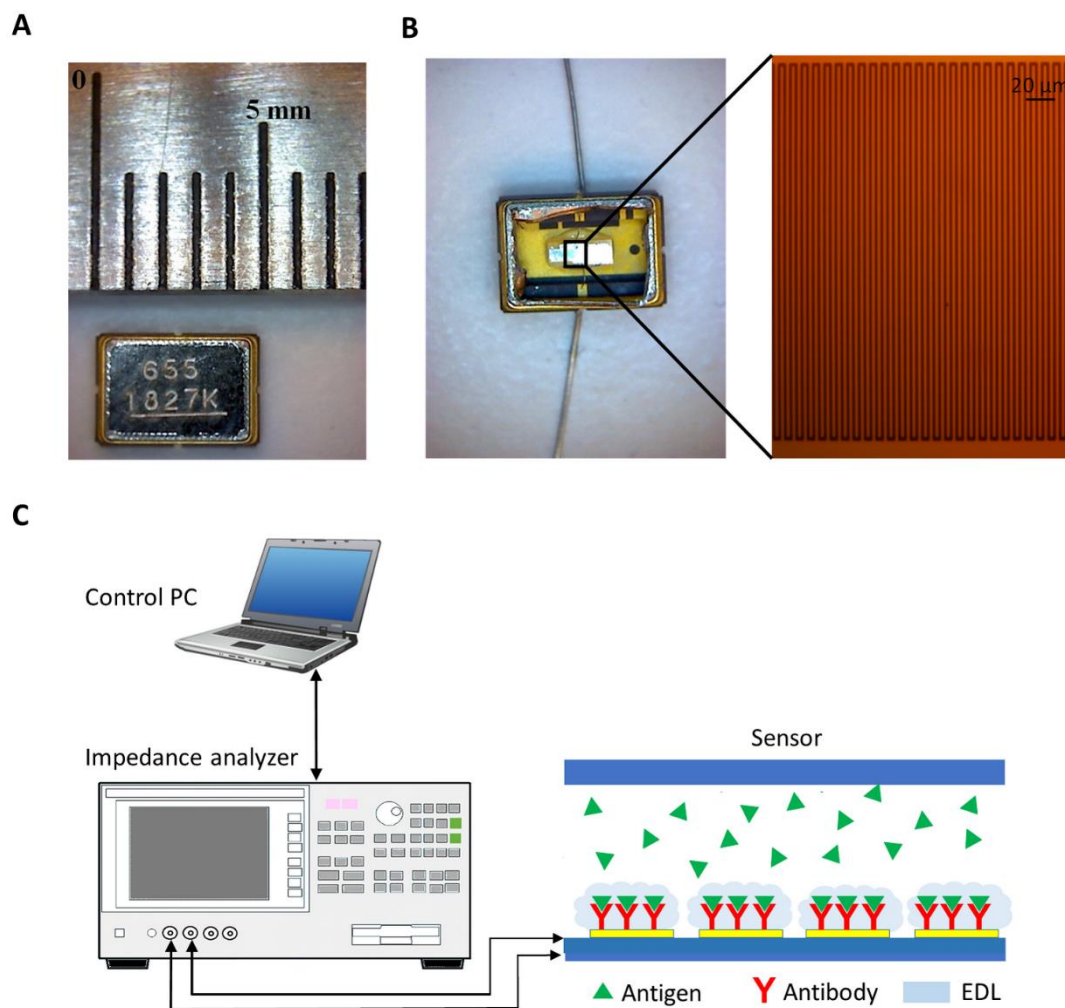


**Figure 3.1.** SAW resonator: **A)** size and **B)** modified chip with the interdigitated electrodes. **C)** Schematic of experimental setup and the detection mechanism.

#### 3.1.4. Sensor specificity and selectivity test

In order to study the specificity of the sensor, IgG-free bovine serum albumin (BSA) diluted with 0.1xPBS (1% BSA) was used as the control buffer and to dilute the anti-bovine IgG. In order to make 1% BSA, 1 g of IgG-free BSA was diluted in 100 mL of 0.1xPBS and well mixed. Then, the anti-bovine IgG was diluted with this buffer to 1 ng/ml and 10 ng/ml concentrations. For selectivity test purposes, 1:20 diluted mouse serum (Jackson ImmunoResearch Laboratories Inc.) with 0.1xPBS was used. The 1 ng/ml and 10 ng/ml

anti-bovine IgG were diluted with mouse serum to test the sensor's selectivity. It should be noted that the supplied bovine IgG had minimal cross-reactivity with mouse serum proteins.

#### 3.1.5. SARS-CoV-2 Nab detection procedure

When the SARS-CoV-2 RBDs are introduced into the biosensors, the RBDs that are neutralized by the NABs will not interact with hACE2 receptors on the electrode surfaces. The non-neutralized RBDs will link to the hACE2 receptors (**Figure 3.2**). The change in the impedance response depends on the amount of interacted RBD-hACE2 on the electrode surface and, thus, a function of the NABs' concentration. To detect NABs, hACE2 proteins were immobilized using NHS-EDC chemistry to interact with RBDs in the sample [46]. The immobilization procedure is as follows. After rinsing the electrode surfaces with ethanol and exposing the surface to plasma for 30 s, electrodes were incubated overnight in alkanethiol solution (99% 11-mercapto-1-undecanol 1 mM and 1% 16-mercaptohexadecanoic acid 1 mM in ethanol). The activated electrodes were rinsed with ethanol and immersed for 30 min inside a solution of 100 mg dimethylaminopropyl carbodiimide and 40mg N-hydroxysuccinimide in 4 mL of DI water. The electrodes were then rinsed with DI water and incubated with 0.1  $\mu\text{g}/\mu\text{L}$  hACE2 protein in PBS. Finally, electrodes were rinsed with PBS and dried. Impedance measurements of the sensors with and without hACE2 immobilization were used to ensure protein deposition on the surface. The device sensitivity was obtained for different NAB concentrations in the buffer. The working principle is: (i) NABs with different concentrations were mixed with SARS-CoV-2 RBD diluted in PBS. (ii) The mixture was loaded and filled into the microchamber. (iii) Sensor surfaces were previously functionalized with the hACE2, and non-neutralized

RBDs interacted with the hACE2 receptors. (iv) Impedance response, which is a function of NAb concentration, was recorded.

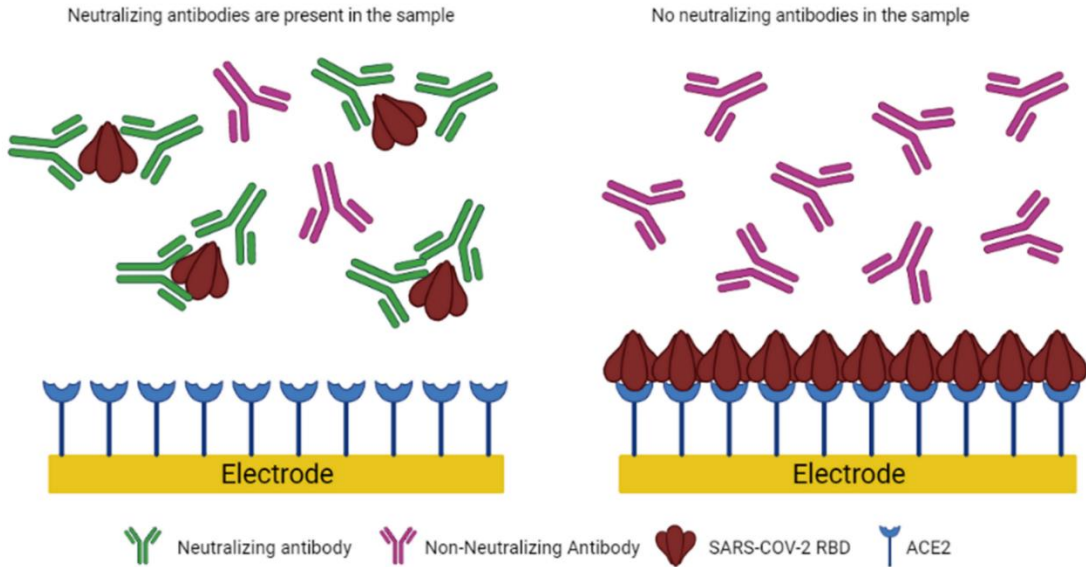


**Figure 3.2.** The schematic detection mechanism for the SARS-CoV-2 specific NAbs.

### 3.2. Results and Discussion

Before characterizing the biosensor detection capability, the optimum applied electric potential and frequency need to be determined. Also, it is important to find whether the surface has been immobilized with bovine IgG or not. Therefore, the impedances of the devices before and after immobilization were recorded at 10, 20, 100, 500, and 1000 mV in a frequency range from 100 Hz to 10 MHz to investigate these parameters. **Figure 3.3** shows the impedance spectra presented in the Bode diagram to illustrate the abovementioned effects.

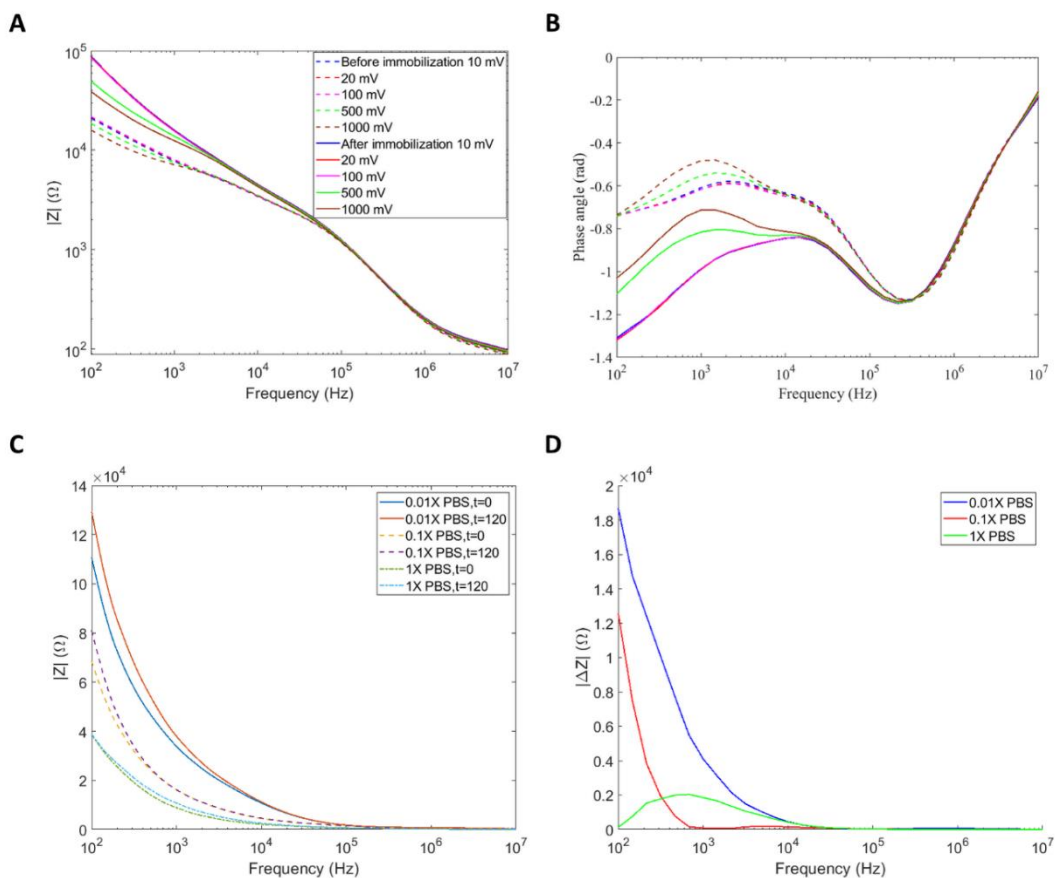


**Figure 3.3.** Voltage and antibody immobilization effects on **A)** impedance magnitude and **B)** phase angle of the chip impedance. **C)** Impedance magnitudes before ( $t=0$ ) and after ( $t=120$  s) antibody-antigen interaction at different PBS concentrations. **D)** Impedance magnitude changes before and after antibody-antigen interaction in the frequency range from 100 Hz to 10 MHz for different PBS dilutions.

System impedances were measured at 10, 20, 100, 500, and 1000 mV in the 100 Hz to 10 MHz range to investigate the effects of the applied potential. **Figures 3.3A** and **3.3B** show the impedance magnitude and phase angle before and after antibody immobilization. Both cases show applied potential dependency up to 1 kHz, beyond which, impedance dependency on the measurement potential vanishes. However, at lower frequency ranges Faradaic reactions become important, exhibiting potential dependent impedance above 100 mV. For this reason, all proceeding measurements were conducted at 100 mV. Comparison

between the magnitudes of the system impedances before and after antibody immobilization in **Figure 3.3A** shows increased impedance after immobilization, which is expected due to the covering of the electrode surfaces with a thin layer of antibody. Especially the phase angles in **Figure 3.3B** up to 1 kHz show mixed resistive and capacitive behavior before immobilization, which is typical of EDL response of bare electrodes. This behavior becomes mostly capacitive due to the thin electrodes being covered by immobilized antibodies, which act like an insulating layer.

To find the effective detection frequency, impedance changes for the maximum anti-bovine IgG concentration for 0.01xPBS (100 ng/ml), 0.1xPBS (100 ng/ml), and 1xPBS (10  $\mu$ g/ml) were obtained from 100 Hz to 10 MHz. **Figure 3.3C** shows the impedance of the chip as a function of frequency 120 s after the anti-bovine IgG was applied to the chamber. This figure demonstrates that the values for the higher PBS dilution (1xPBS) are lower due to the decrease in the solution resistance. **Figure 3.3D** shows impedance changes after 120 s for each buffer dilution. According to this figure, for 0.01xPBS and 0.1xPBS, 100 Hz is the frequency at which the impedance changes are maximum. However, for 1xPBS, this frequency is about 600Hz. Based on this outcome, the LOD of the chip was investigated in these specified frequencies as a function of the used anti-bovine IgG concentration.

With applying proper voltage and frequency, the LOD of the device in different concentrations of PBS buffer with conductivities of  $\sim 0.016$ ,  $\sim 0.16$ , and  $\sim 1.6$  S/m are investigated. **Figures 3.4A** and **3.4B** show anti-bovine IgG detection with 1, 10, and 100 ng/ml concentrations at 100 mV and 100 Hz at 0.01xPBS and 0.1xPBS, respectively. The impedance response increases with increased antigen concentrations, as expected. **Figure 3.4C** illustrates LOD for anti-bovine IgG in 1xPBS ( $\sigma \sim 1.6$  (S/m)), where the measurements

are meaningful for antigen concentration of 10  $\mu\text{g/ml}$ . **Figure 3.4D** shows standard deviations (STDs) for these cases, determining LOD for all cases. Based on the Analysis of Variance (ANOVA) test, the minimum detections for 0.01xPBS, 0.1xPBS, and 1xPBS are 1 ng/ml, 10 ng/ml, and 10  $\mu\text{g/ml}$ , respectively. Detection at lower antigen concentrations is possible only for diluted samples. For example, 100 times dilution allows 1 ng/ml detection in 0.01xPBS, while 10 times dilution can detect 10 ng/ml in 0.1xPBS. This means that a physiological sample of 1.6 S/m conductivity needs to be diluted 10 to 100 times to detect the antigen, making the LOD for the actual sample (prior to the dilutions) 100 ng/ml for 0.1xPBS and 0.01xPBS. The main reason for such a low LOD for 1xPBS is that  $\lambda_d$  thickness is about 0.7 nm, which is smaller than IgG antibody ( $\sim 10$  nm), so EDL change after the interaction is small [34]. Also, in high conductive solutions (e.g., biological samples) and low frequencies, Electrode Polarization (EP) effect can overshadow the recorded signal. Reducing this adverse effect can improve the LOD of interdigitated electrodes in high conductivity buffers.

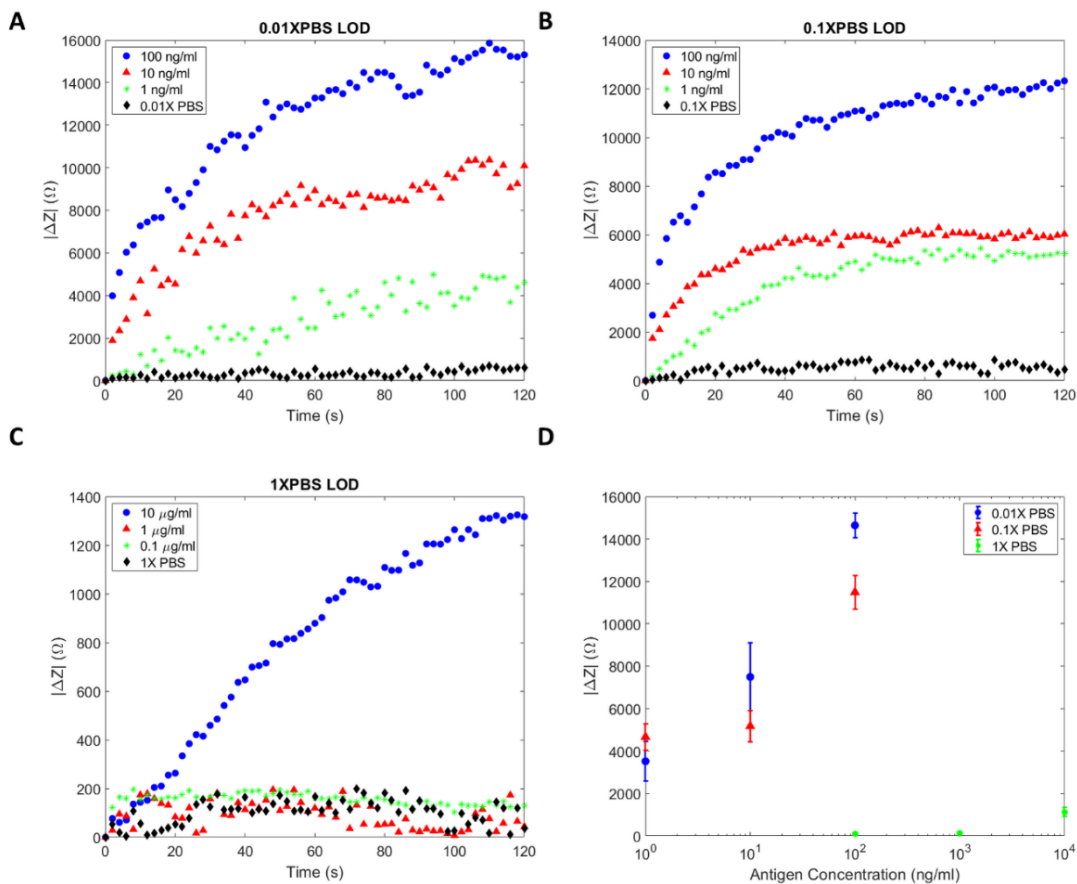


**Figure 3.4.** Detection of different antigen concentrations in **A)** 0.01xPBS buffer, **B)** 0.1xPBS buffer, and **C)** 1xPBS buffer. **D)** Standard deviation of LOD for each PBS buffer. All data for 0.01xPBS and 0.1xPBS were obtained at 100 mV and 100 Hz. For 1xPBS, the data was obtained at 100 mV and 600 Hz.

Specificity and selectivity are necessary considerations for biosensor development. Specificity shows that the antibody only recognizes and binds to a specific antigen, whereas selectivity is the ability to differentiate the intended target molecule within a complex mixture. In order to test specificity of the sensor IgG-free BSA was used as the control buffer at 0.1xPBS. The IgG-free BSA buffer was also used to prepare the anti-bovine IgG buffers with 1 (ng/ml) and 10 (ng/ml) concentrations. **Figure 3.5A** demonstrates no detection with the current sensor when the control buffer was applied. However, adding

anti-bovine IgG at various concentrations results in detection similar to that in **Figure 3.4B**. To determine the sensor's selectivity, mouse serum was used as the complex control buffer, and anti-bovine IgG with 1 (ng/ml) and 10 (ng/ml) were added to this buffer. **Figure 3.5B** proves the potential of the sensor to discriminate the anti-bovine IgG from the mouse serum IgGs, and shows a good target-specific response for different antigen concentrations.

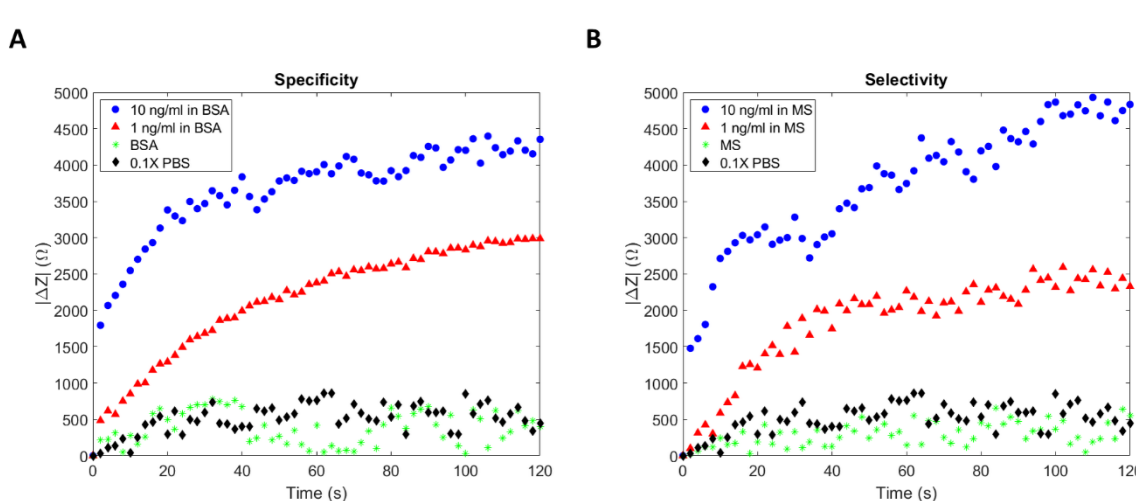


**Figure 3.5.** Detection of different antigen concentrations in **A)** IgG-free BSA and **B)** Mouse serum (MS) to study specificity and selectivity of detection, respectively. All data were obtained for 0.1xPBS at 100 mV and 100 Hz.

ACEK phenomena are widely reported to enhance detection in electrochemical immunoassay biosensors. It is important to understand the relative effects of ACEK forces on the sensor performance. To determine the dominant transport mechanism in the device, the order of magnitudes for reagent displacement in 1 s due to the ACEK phenomena (ACEO, ACET, and DEP) and Brownian motion were obtained using **Equations 2.1 to 2.5**. The most effective voltage and frequency for each PBS dilution were used. According to the results shown in **Table 3.1**, Brownian motion is the dominant transport phenomenon in the sensor system. In other words, device detection is mainly diffusion-based instead of

ACEK-based. Therefore, to improve the detection capabilities of the ACEK device, the operational conditions or design must be altered to amplify these effects. To clarify this outcome, antibody-antigen binding has also been simulated in a pure diffusion condition, and the concentration results are shown in **Figure 3.6**.

**Table 3.1.** Reagent displacement in the device due to the ACEO, ACET, DEP, and Brownian motion in 1 (s).

	0.01XPBS (m/s)	0.1XPBS (m/s)	1XPBS (m/s)
ACEO	$9.73 \times 10^{-12}$	$3.64 \times 10^{-14}$	$1.12 \times 10^{-16}$
ACET	$2.22 \times 10^{-11}$	$2.22 \times 10^{-10}$	$2.22 \times 10^{-9}$
DEP	$3.92 \times 10^{-16}$	$5.91 \times 10^{-22}$	$-1.11 \times 10^{-23}$
Brownian motion	$9.35 \times 10^{-7}$	$9.35 \times 10^{-7}$	$9.35 \times 10^{-7}$

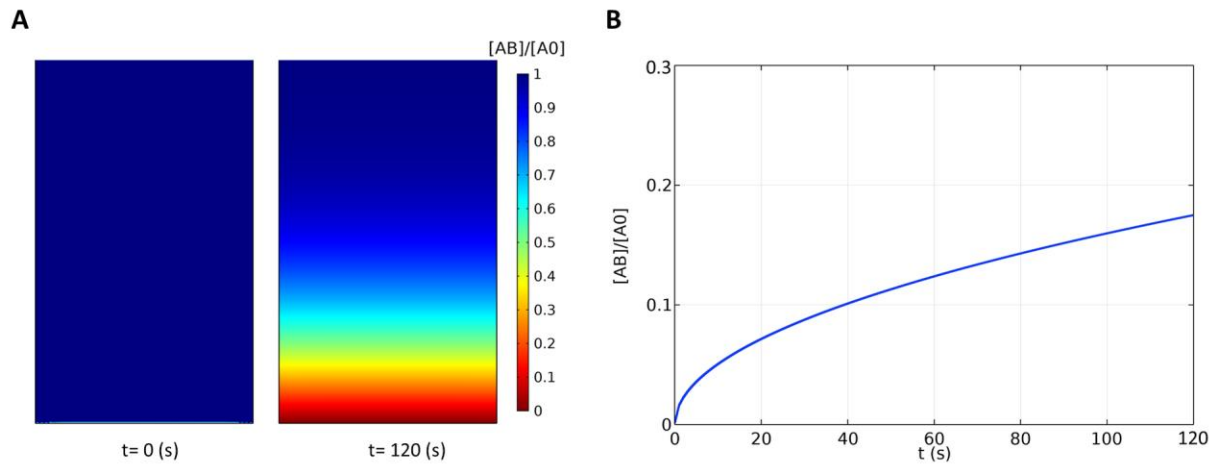


**Figure 3.6.** Concentration results from simulations. **A)** Contour plot of the normalized anti-bovine IgG concentration ( $[AB]/[A_0]$ ) at the initial time ( $t=0$ ) and ( $t=120$  s). **B)** Normalized concentration of the interacted anti-bovine IgG-bovine IgG ( $[AB]/[A_0]$ ) on the surface of the electrodes.

**Figure 3.6A** shows normalized anti-bovine IgG concentration ( $[A]$ ) at the initial time ( $t=0$ ) and after 120 s of antibody-antigen reaction. This figure shows that antigen concentration reduces near the electrode surface due to interacting with the antibodies on the surface.

**Figure 3.6B** shows the normalized concentration for the reacted protein-protein ( $[AB]$ ) on the electrode surface. According to the simulation, diffusion base interaction has the same trend as the changes in impedance. The abovementioned impedance changes are mainly because of the electric isolation layer when the proteins with different dielectric properties cover the electrode surface. The impedance increases as the thickness of this layer increases (**Figure 3.4**).

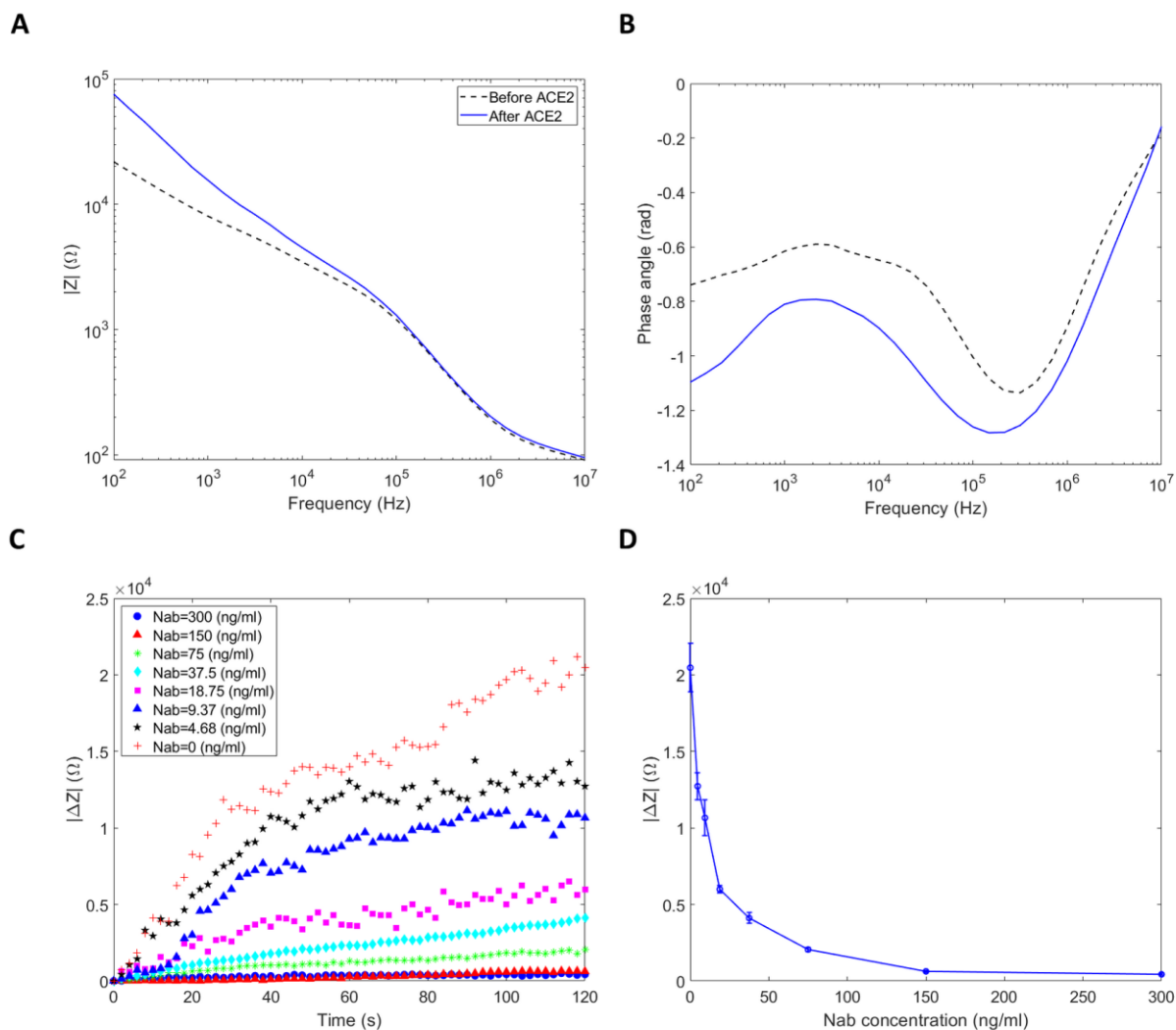


**Figure 3.7.** ACE2 immobilization effects on **A)** impedance magnitude and **B)** the phase angle of the chip impedance. **C)** LOD for RBD-hACE2 interaction for different NAb concentrations. **D)** The NAb concentration and impedance change relationship for the device. All data were obtained using 0.1xPBS buffer for dilution at 100 mV and 100 Hz.

We next investigate the capability of the sensor to detect SARS-CoV-2 RBD NAb. After immobilizing the electrode surface with hACE2 protein, 0.1xPBS solutions with specific NAb concentrations were applied to the device and the changes in impedance were recorded. The immobilized devices with hACE2 were connected to the impedance analyzer to record the impedance with the applied voltage of 100 mV at 100 Hz. **Figure 3.7A** shows

the impedance increase at low frequencies, and **Figure 3.7B** shows more capacitive behavior of the impedance after hACE2 immobilization on the surface. This change in the impedance is due to the electrode surface coverage by hACE2, which changes the surface electrical properties. However, when the SARS-CoV-2 RBD solution was introduced into the sensor, RBDs would interact with the hACE2 receptors on the surface. Due to this interaction, EDL thickness would change, which results in the impedance increase. However, NAb prevent this interaction by deactivating the viral RBDs (**Figure 3.2**). Therefore, depending on the NAb concentrations in a RBD buffer, the impedance responses become different. If enough NAb were in the RBD solution, there would be no RBD-hACE2 interaction on the surface. Consequently, there would be no impedance change. **Figure 3.7C** demonstrates the results of RBD-hACE2 interaction in presence of NAb with different concentrations, obtained from serial dilution of the 300 ng/ml NAb solution [6]. According to this figure, when the applied NAb concentration to the device increased, there was less interaction between the RBDs and hACE2 on the electrode surface, so there was almost no change in impedance. However, when RBDs were not neutralized (such as in the case of a low concentration of NAb), more RBD and hACE2 interaction occurred on the electrode surface, resulting in greater impedance changes.

Each experiment is repeated three times, and **Figure 3.7D** shows an average detection curve for this device based on the impedance changes for the known concentrations of the NAb in the RBD buffer. The impedance change ( $|\Delta Z|$ ) was calculated from the sensor impedance after ACE2 immobilization ( $t=0$ ) and  $t=120$  s after applying the RBD buffer with NAb. This curve can be used to determine the concentration of NAb in any sample since it covers the concentration range of the analytical measuring interval (AMI). In other

words, a sample with an unknown NAb concentration can be introduced into the sensor. The NAb concentration can be estimated from the resultant impedance change curve in **Figure 3.7D**. The demonstration shows feasibility for a label-free detection with less time and cost, making it more applicable for point-of-care detection compared to ELISA methods [6].

### 3.3. Conclusion

In the present study, the capability of a biosensor to detect IgG protein was investigated using the impedance spectroscopy method. First, experimental parameters were determined, including applied AC voltage and frequency. The impedance spectrum for the device in a frequency range from 100 Hz to 10 MHz showed that the impedance represented buffer resistance in higher frequencies. There is no significant change in impedance in the frequency range from 10 kHz to 10 MHz. Impedance changes mostly happened in lower frequencies, and maximum change occurred at 100 Hz. Therefore, the optimum detection frequency was expected to place in the low-frequency range. To find the most effective frequency for detection, binding was studied in the same frequency range for each buffer solution in which the maximum interaction occurred at 100 Hz for 0.01xPBS and 0.1xPBS. For 1xPBS, the optimum frequency was found to be around 600 Hz. Then, the most effective applied AC magnitude was determined.

The effect of different applied AC voltages (less than 1  $V_{pp}$ ) was recorded on the device's impedance. Results illustrated that impedance was reduced in applied voltages larger than 500 mV. Therefore, to eliminate this side effect on the impedance change due to the

binding, a 100 mV voltage amplitude was applied to the sensor. To investigate the binding efficiency of the device, anti-bovine IgG and bovine IgG interaction in three different PBS buffers of 0.01xPBS ( $\sigma \sim 0.016$  (S/m)), 0.1xPBS ( $\sigma \sim 0.16$  (S/m)), and 1xPBS ( $\sigma \sim 1.6$  (S/m)) were studied. ANOVA test was used to determine LODs for different mentioned dilution buffers. The results demonstrated 1 (ng/ml), 10 (ng/ml), and 10 ( $\mu\text{g/ml}$ ) LOD for 0.01xPBS, 0.1xPBS, and 1xPBS, respectively. Also, in previous studies, ACEK phenomena were introduced as the dominant mechanism in such a device. Due to low electric potential magnitudes, transport in the device is dominated by Brownian motion, as shown by the scaling analysis. Therefore, the detection happens mainly due to diffusion rather than ACEK transport. Numerical simulations of diffusive interactions show similar trends with the experimental data.

As an application, the present interdigitated electrode was used to detect SARS-CoV-2 neutralizing antibodies. The hACE2 receptors which interacted with RBDs were immobilized on the electrode surface. RBS buffers with different NAb concentrations were applied to the device. The results showed that in high NAb concentrations, RBDs were neutralized, and there was no interaction on the electrode surface. Therefore, impedance showed almost no change. However, in low NAb concentrations, RBDs bound to the hACE2, and the impedance changes illustrated this interaction. The device has the potential to be fast, inexpensive, and easy to operate, and provide a quantitative assessment of neutralizing antibodies in samples.

## Chapter 4

### COMPETING EFFECTS OF BUOYANCY-DRIVEN AND ELECTROTHERMAL FLOWS FOR JOULE HEATING-INDUCED TRANSPORT IN MICROCHANNELS

Ionic fluids subjected to externally applied electric fields experience Joule heating, which increases with the increased electric field and ionic conductivity of the medium. Temperature gradients induced by Joule heating can create buoyancy-driven flows produced by local density changes, as well as electrothermal transport due to the temperature dependent variations in fluid permittivity and conductivity. This manuscript considers Joule heating induced transport in microchannels by a pair of electrodes under AC electric fields. Resulting buoyancy-driven and alternating current electrothermal (ACET) flows are investigated theoretically, numerically, and experimentally. Proper normalizations of the governing equations led to the ratio of the electrothermal and buoyancy velocities, as a new non-dimensional parameter, which enabled the construction of a phase-diagram that can predict the dominance of ACET and buoyancy driven flows as a function of the channel size and electric field. Numerical results were used to verify the phase-diagram in various height microchannels for different ionic conductivity fluids and electric fields, while the numerical results were validated using the micro-particle-image velocimetry technique. The present study brings insights into Joule heating-induced transport phenomena in microfluidic devices and provides a pathway for the design and utilization of ACET-based devices by properly considering the co-occurring buoyancy driven flow.

## 4.1. Materials and Methods

### 4.1.1. Numerical simulation

In this work, **Equation 2.9**, **Equation 2.12**, **Equation 2.14**, and **Equation 2.22** are coupled and solved using COMSOL Multiphysics software. The temperature dependent material properties for water and glass were used from the software's material library. Heat Transfer, Electrostatics, and Laminar Flow (neglecting the inertial term due to Stokes flow assumption) modules are considered to model the Joule heating-based transport phenomenon. The electric force is added as volume force in the Laminar Flow, and non-isothermal flow coupling is included to solve Laminar Flow and Heat Transfer together.

COMSOL employed finite element method (FEM) to find a numerical solution to the coupled PDEs for the momentum, energy, and electric field. This software applies Newton-Raphson method to linearize these nonlinear equations, which creates a system of linear equations that are solved by MUMPS (MULTifrontal Massively Parallel Sparse Direct Solver). MUMPS perform factorization of the coefficient matrix into a product of matrices, using a method known as LU decomposition, where L is a lower triangular matrix and U is an upper triangular matrix. The LU decomposition allows the solution of the linear system of equations to be performed efficiently, by first solving the two triangular systems  $Ly = b$  and  $Ux = y$ .

In order to improve the accuracy of the solution, the nonlinear solver performs iterations. Then, the values of the variables at each iteration are updated based on the results of the previous iteration. The solution is assumed to be converged when the changes in the values of the variables are below the tolerance (convergence criterion). The default convergence

criterion for heat transfer is set to  $1e-6$ , meaning that the simulation will stop when the relative error falls below  $1e-6$ . A smaller convergence criterion will require more computational time. On the other hand, a larger convergence criterion will result in faster simulations, but may not provide accurate results. Therefore, the default convergence criterion was used for modeling to avoid either high computational costs or low accurate results.

Beside the iterations, it is important to find proper number of nodes (mesh densities) to ensure that the results of the FEM analysis are mesh independent. **Figure 4.1A** shows a schematic model of the computational domain. Mesh independency test performed for the case of  $H=300\ \mu\text{m}$ ,  $\sigma=1.2\ \text{S/m}$ , and  $\phi=7\ \text{V}_{\text{pp}}$  with triangular elements (**Figure 4.1B**) starting with a coarse mesh first and then refining the mesh to get a more accurate solution. **Figure 4.1C to Figure 4.1E** demonstrates flow stabilization for different mesh sizes. This figure also shows the velocity distribution has no significant change in mesh sizes higher than 969,660. According to the results, increasing number of elements more than 969,660 result in less than 4% change in the maximum velocity magnitude in the channel (**Figure 4.1F**). Besides, the computational time is 30 times more when the number of elements increase from 969,660 to 2,806,012 on a PC with 32 GB RAM and a Core i7 CPU. Therefore, about 969,660 elements were selected for all simulations in this chapter to reduce the computational costs.

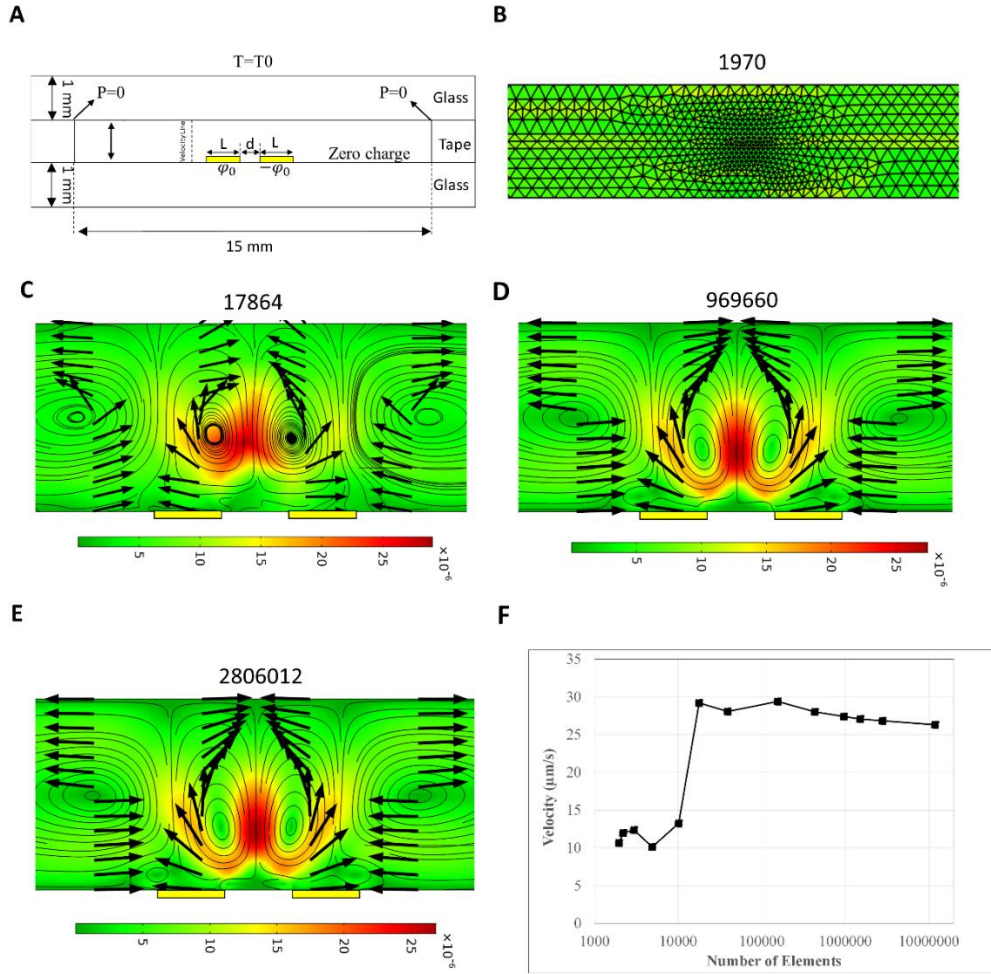


**Figure 4.1.** **A)** the triangular grid produced by COMSOL in the computational domain. **B)** Maximum velocity magnitude induced in the fluid when  $H=300 \mu\text{m}$ ,  $\sigma=1.2 \text{ S/m}$ , and  $\varphi=7 V_{pp}$  for different number of grids. Speed contours, velocity vectors and the streamlines in the domain with **C)** 17864, **D)** 156592, **E)** 969660, **F)** 2806012 number of elements.

#### 4.1.2. Device fabrication and experimental setup

Standard photolithography techniques were used to fabricate the devices used for experiments. This method has been widely used in our group to develop microfluidics devices for different applications such as cell screening [47], cell characterization [37], detection [26], particle trapping [32], and electro-polarization effect reduction [48, 49] in high conductive buffers. First, glass slides with dimensions of  $25 \text{ mm} \times 25 \text{ mm} \times 1 \text{ mm}$

were washed in three steps with 1M KOH, acetone, and isopropyl alcohol, in an ultrasonic bath (FB11201, Fisher Scientific, Waltham, MA, USA) in 25°C and 37 kHz operation condition. Between each step, the glass slides were washed with deionized (DI) water from the Millipore Alpha-Q water system (Bedford, MA, USA). After washing, they were dried with nitrogen and kept in an oven (20GC Lab Oven, Quinvy Lab Inc.) at 150°C for 20 minutes to fully dry them. Afterward, they were cooled down to room temperature, and a positive photoresist (S1813) was coated on the surface using a spin coater. Multistage rotation speed was selected on the device to have a smooth layer of the photoresist (1,000 rpm and 4,000 rpm for 10 s and 30 s, respectively, with 300 rpm/s acceleration/deceleration stages). Then, the coated substrates were soft-baked for 1 min at 115°C on a hot plate. Afterward, 110 mJ/cm<sup>2</sup> UV light was applied to the substrate covered with a designed transparency mask using a mask aligner (Karl Suss, MJB3). The UV-treated substrates were immersed in a developer solution (MF-26A) to remove the UV-exposed areas. This is followed by the deposition of a 3 nm Chromium layer and 22 nm gold layer on the surface of the glass slides using a sputter coater (EMS300TD, Emitech), and the unexposed photoresist and metal layers on top of it were lifted off from the surfaces by submerging them in PG remover solution at 80°C. After electrode fabrication, a copper tape was attached to the electrode tips to apply an electric field. The microchannels were made by cutting a 50 µm thick double-sided tape with 15 mm × 3 mm dimensions using a craft cutter (Silver Bullet). The tape layers between the electrode substrate and a cover glass placed above the double-sided tape determined the microchamber height. **Figure 4.2A** shows the fabricated device. Specific amounts of KCl were used to adjust the ionic conductivity of water in the experiments, while polystyrene particles (PS) immersed in

these buffers were used for flow visualization under a microscope (IX81, Olympus). The flow field was recorded by Hamamatsu digital camera C11440 connected to a computer. The AC signal was applied to the device using a function generator (AFG 3102, Tektronix). An oscilloscope (TDS 2014B) was also used to ensure the applied voltage and frequency accuracy. **Figure 4.2B** shows the experimental setup.

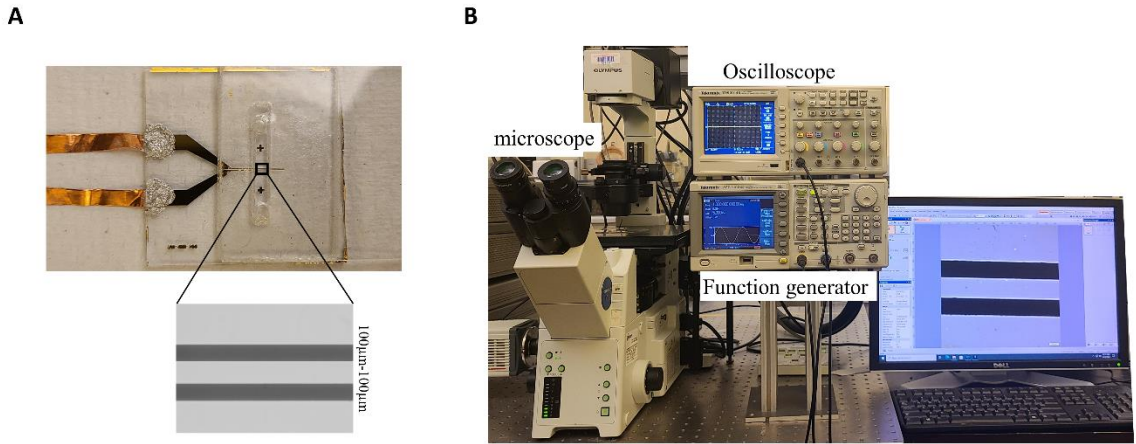


**Figure 4.2.** A) Fabricated device using the photolithography method, B) Experimental setup.

#### 4.1.3. Particle image velocimetry (PIV)

The velocity field near the electrode region within the flow is measured using the particle image velocimetry (PIV) technique. A KCl solution with a conductivity of 1.2 S/m was seeded with 1  $\mu\text{m}$  PS particles (SIGMA-ALDRICH) at 2% V/V for experiments. The snapshots were taken by a 20X objective (LUCPLFL) with a 50 ms exposure time using cellSens imaging software. The image calibration is 0.25  $\mu\text{m}/\text{px}$ . The velocity field was calculated using the PIVLab MATLAB code in an interrogation area of 64 $\times$ 64 pixels [50]. The velocity field was measured at a focal region 70  $\mu\text{m}$  above the bottom of the electrode surface.

The PIV technique is limited by the diffraction of light. The diameter of the diffraction-limited point spread function determines the PIV precision ( $d_s$ ).

$$d_s = 2.44M \frac{\lambda}{2NA} \quad (4.1)$$

where  $M=20$  is the magnification,  $\lambda \sim 500$  nm is the light source wavelength,  $NA=0.45$  is the objective lens numerical aperture, and  $d_s$  is the effective particle diameter. According to the light source and the objective lens,  $d_s$  is approximately  $27 \mu\text{m}$  from **Equation 4.1**. Also, the actual image recorded by the CCD camera combines the diffraction-limited image and the geometric image. The diffraction-limited image is the ideal image with a perfect system, but the geometric image is the image captured by the optical system, including optical imperfections. Approximating these two images, the effective particle diameter  $d_e$  can be obtained from:

$$d_e = [M^2 d_p^2 + d_s^2]^{\frac{1}{2}} \quad (4.2)$$

Considering  $1 \mu\text{m}$  particle diameter, the effective particle diameter  $d_e$  is  $\sim 33 \mu\text{m}$ . This order of magnitude for  $d_e$  is also reported in other PIV measurement setups [29, 31, 51]. When a particle image diameter is resolved by 3-4 pixels (our particles are  $1 \mu\text{m}$  and the acquired image pixel size is  $0.25 \mu\text{m}$ ), the particle displacement accuracy can be calculated from  $\delta_x = \frac{d_e}{10M}$  [52]. Therefore, for our setup,  $\delta_x$  is in the order of  $100$  nm, which means the particle displacement measurement using the present experimental setup is accurate within  $100$  nm [51].

## 4.2. Results and Discussion

This section presents acquired results from the theoretical analysis, simulations, and experimental methods. We first validate the numerical results with the experimental data available in the literature [31]. Also, there are some main references in the literature which serve as a simulation guide for Joule heating based transport phenomena [29, 30, 53, 54]. In these articles, the Boussinesq approximation was used to describe buoyancy force in the momentum equation. However, the force term was suggested as  $\mathbf{F}_b = \rho_0\beta(T - T_0)\mathbf{g}$ . According to **Equation 2.22**, the correct force term is  $\mathbf{F}_b = -\rho_0\beta(T - T_0)\mathbf{g}$ . Here, we show the differences in the previous model and the correct simulation model.

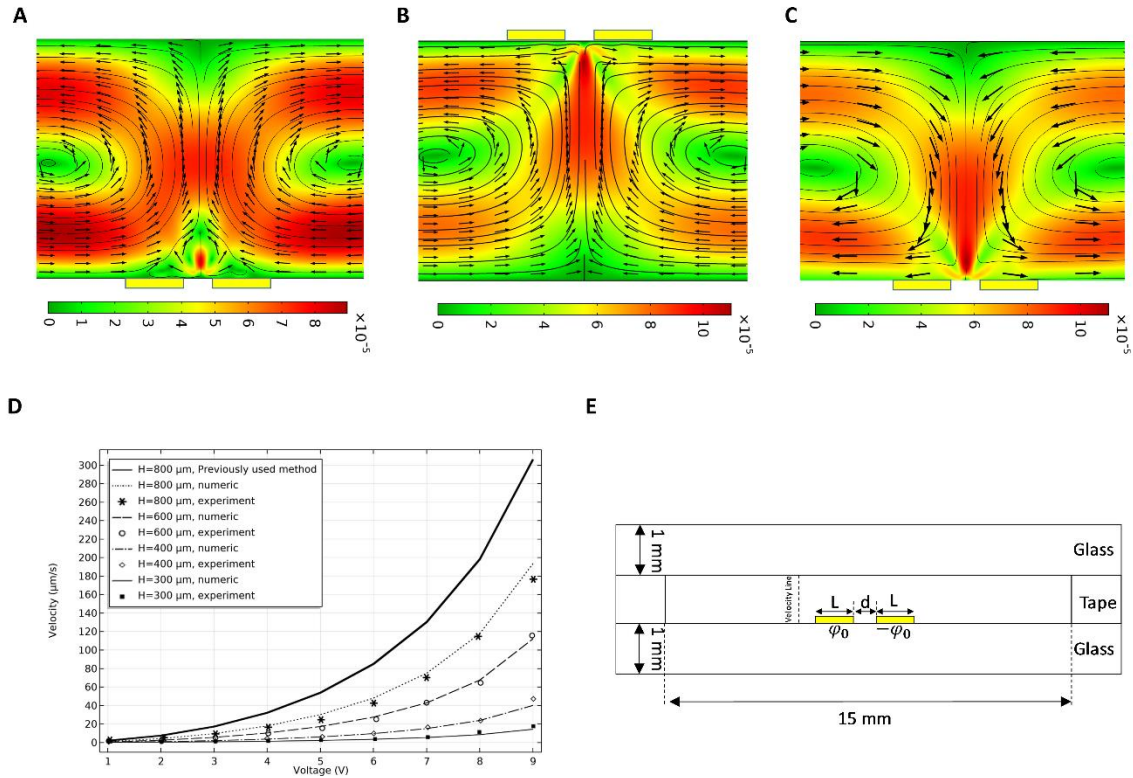


**Figure 4.3.** Streamlines, velocity vectors, and the speed contours obtained for Joule heating induced transport in a microchannel with electrodes placed at the bottom (**A**) and top (**B**) of the channel. The gravitational acceleration is downwards. **C**) Streamlines, velocity vectors, and the speed contours obtained for Joule heating induced transport in a microchannel with electrodes placed at the bottom with upward gravitational acceleration. A portion of the simulation domain is shown, while the used geometry ( $L= 100 \mu\text{m}$  and  $d=50 \mu\text{m}$ ), applied voltage ( $7 V_{pp}$ ), and the ionic conductivity of the fluid ( $\sigma=1.2 \text{ S/m}$ ) were matched with the values reported in [31]. **D**) Simulation results compared with the experimental data in [16] and previously used model, **E**) A schematic view of the simulated and fabricated device.

**Figure 4.3A** and **Figure 4.3B** show the streamlines, velocity vectors, and speed contours for Joule heating induced transport in  $50 \text{ mm} \times 10 \text{ mm} \times 0.8 \text{ mm}$  microchannel with two  $100 \mu\text{m}$  electrodes that are separated by  $50 \mu\text{m}$  distance. The simulations were conducted at  $\varphi = 7 V_{pp}$  electrode potential and for  $\sigma=1.2 \text{ S/m}$  ionic conductivity. The used geometry, electrode dimensions, and simulation conditions are chosen to be similar to the experimental conditions reported in [31]. Although the entire domain is simulated, the flow

field near the electrode region is presented. **Figure 4.3A** shows the simulation results for a pair of electrodes placed on the bottom of the channel, similar to the experiments in [31]. In this configuration, the local temperature will be increased near the electrodes due to Joule heating, leading to lower density fluid near the electrodes rising due to the buoyancy effects. However, the electrothermal force generates two small downward vortices between the electrodes, clearly showing *competition* between the buoyancy driven and electrothermal flows in this configuration. **Figure 4.3B** shows the flow field when the electrodes are placed on top of the channel. The hot spot between the two electrodes due to Joule heating is at the top of the domain. The resulting electrothermal flow creates two upward vortices in the same direction with the resulting buoyancy driven flow, *enhancing* each their combined effects. **Figure 4.3C** shows simulation results using **Equation 2.22** with  $\rho_0\beta(T - T_0)\mathbf{g}$  on the RHS instead of the correct  $-\rho_0\beta(T - T_0)\mathbf{g}$  term. The sign error in **Equation 2.22** leads to a body force towards bottom of the domain under a downwards gravitational force field. However, having electrodes at the bottom of the channel will increase the local temperature near the electrodes, leading to lower density fluid near the electrodes that will rise up due to the buoyancy effects. Simply this sign error results in the wrong direction of the flow.

Using a pair of electrodes on the bottom of the channel is the most common configuration in microfluidics applications. As we will show next, there is a competing effect of the electrothermal and buoyancy driven flows in general for electrodes on the bottom of the channel. For the case shown in **Figure 4.3**, the buoyancy driven flow dominates over ETF, with the exception of the local circulatory pattern between the two electrodes near the bottom of the domain. It is important to validate these results with the experimental data.

For this purpose, we present in **Figure 4.3D** the flow speeds obtained by Lu et al. [31] using the micro particle image velocimetry technique in a similar microchannel system with channel heights varying from 300  $\mu\text{m}$  to 800  $\mu\text{m}$ . Specifically, the velocity profiles were measured 500  $\mu\text{m}$  away from the edge of the electrodes and 100  $\mu\text{m}$  above the bottom of the channel surface under varying applied electric potentials. The figure also shows fluid speeds at the same location of the experiments under varying electric potentials, using the formulation in **Equation 2.22**. The figure also includes the “previously used method” data shown by the solid line for the 800  $\mu\text{m}$  height channel. This data was obtained using the incorrect simulation procedure suggested in the literature [29], which significantly overestimates the computed fluid velocity. This type of Joule heating based flow motion has been reported widely in the literature. There are only a few references [23, 31], in which, correct flow was simulated and reported. To further simplify the experimental and numerical procedure, the geometry and materials shown in **Figure 4.3E** were used in the rest of this article.

Results from **Figure 4.3** clearly indicate the importance of distinguishing the relative magnitudes of the electric field ( $\mathbf{F}_e$ ) and buoyancy ( $\mathbf{F}_b$ ) effects in **Equation 2.22**, which determines the resulting flow field in the microchannels. For this purpose, we present the proper non-dimensionalization of the energy and momentum equations that result in mixed electrothermal and buoyancy driven flows in microchannels. Overall, the steady Stokes and energy equations are non-dimensionalized by choosing the characteristic length scales and parameters listed in **Table 4.1**.

**Table 4.1.** Characteristic parameters used for non-dimensionalization of the steady Stokes and energy equations.

Variable	Expression	Parameter
Length	$x^* = \frac{x}{L_c}, y^* = \frac{y}{L_c}$	$L_c$ , Characteristic length
Electric potential	$\varphi^* = \frac{\varphi}{\varphi_0}$	$\varphi_0$ , Applied potential
Temperature	$T^* = \frac{T - T_r}{\Delta T}$	$T_r$ , Ambient temperature $\Delta T$ , Characteristic temperature change
Velocity	$u^* = \frac{u}{U_c}$	$U_c$ , Characteristic velocity
Pressure	$P^* = \frac{P - P_r}{\mu \frac{U_c}{L_c}}$	$P_r$ , Reference pressure
Electric permittivity	$\varepsilon^* = \frac{\varepsilon}{\varepsilon_r}$	$\varepsilon_r$ , reference permittivity

Using these parameters, the non-dimensionalized energy equation is given by

$$\nabla^{*2} T^* - \frac{\sigma \varphi_0^2}{k_m \Delta T} (\mathbf{E}^* \cdot \mathbf{E}^*) = 0 \quad (4.3)$$

In this equation, the applied electric potential ( $\varphi_0$ ), thermal ( $k_m$ ) and ionic conductivities ( $\sigma$ ) of the fluid become important along with a characteristic temperature  $\Delta T$  change and a reference temperature  $T_r$ , which is considered 293.15 K. All spatial gradients are

normalized using a single characteristic dimension of  $L_c$ . The non-dimensionalized steady Stokes equations are given by

$$-\nabla^* P^* + \nabla^{*2} \mathbf{u}^* + \frac{c_\sigma \Delta T \varepsilon_r \varphi_0^2}{\mu L_c U_c} \mathbf{F}_e^* + \left(\frac{Gr}{Re}\right) T^* = \mathbf{0} \quad (4.4)$$

Re is the Reynolds number ( $\frac{\rho_0 U_c L_c}{\mu}$ ), and Gr is the Grashof number ( $\frac{\rho_0^2 g \beta \Delta T L_c^3}{\mu^2}$ ). For further simplifications, we define the characteristic temperature change,  $\Delta T$ , and the characteristic velocity,  $U_c$ , in the following forms:

$$\Delta T = \frac{\sigma \varphi_0^2}{k_m} \quad (4.5)$$

$$U_c = \frac{\rho_0 g \beta \Delta T L_c^2}{\mu} \quad (4.6)$$

Substituting the above definitions, the energy and momentum equations are given as follows:

$$\nabla^{*2} T^* - (\mathbf{E}^* \cdot \mathbf{E}^*) = 0 \quad (4.7)$$

$$-\nabla^* P^* + \nabla^{*2} \mathbf{u}^* + \frac{c_\sigma \varepsilon_r \varphi_0^2}{\rho_0 \beta g L_c^3} \mathbf{F}_e^* + T^* = \mathbf{0} \quad (4.8)$$

According to the literature [33], the ETF velocity ( $U_e$ ) arising from the  $\mathbf{F}_e$  term in **Equation 2.22** is proportional to

$$U_e \propto \frac{|M_f|}{T} \frac{\varepsilon \sigma \varphi_0^4}{\mu L_c k_m} \quad (4.9)$$

Where

$$M_f = \frac{(c_\sigma - c_\varepsilon) T}{1 + \left(\frac{2\pi f \varepsilon}{\sigma}\right)^2} + \frac{1}{2} c_\varepsilon T \quad (4.10)$$

which determines the direction and strength of the ETF vortices depending on the relative influences of the electrostatic and dielectric forces on the fluid. When  $M_f < 0$  ( $\frac{2\pi f \varepsilon}{\sigma}$ ) the two rolls above the electrodes create an upward flow. Conversely, When  $M_f > 0$  ( $\frac{2\pi f \varepsilon}{\sigma}$ ), the directions of the vortices are reversed, resulting in a downward flow. In most microfluidic applications, the applied frequency is in the MHz range. Therefore,  $M_f > 0$  and the ETF vortices are towards the electrode gap. Also, the magnitude of these vortices is scaled as  $U_e \propto \frac{c_\sigma \Delta T \varepsilon_r \varphi_0^2}{\mu L_c}$  [33].

In the meantime, the buoyancy driven fluid velocity  $U_b$  in **Equation 2.22** arising from the  $F_b$  term scales as  $U_b \propto \frac{\rho_0 g \beta \Delta T L_c^2}{\mu}$ . Therefore, the non-dimensional number that appears before the  $F_e^*$  in **Equation 4.8** can be defined as the velocity ratio arising from the  $F_e$  and  $F_b$

$$\frac{\text{Electrothermal Velocity}}{\text{Bouyancy Velocity}} = \frac{U_e}{U_b} \propto \frac{c_\sigma \varepsilon_r \varphi_0^2}{\rho_0 \beta g L_c^3} \quad (4.11)$$

The ratio of the velocities in **Equation 4.11** depends only on the characteristic length ( $L_c$ ) and the applied electric potential ( $\varphi_0$ ). In other words, the dominance of  $F_e$  versus  $F_b$  in the flow field is determined by  $L_c$  and  $\varphi_0$ . We performed a series of numerical simulations to decide on the proper length scale for normalization. Among the channel length, height, electrode spacing, and electrode length, we determined that the channel height ( $H$ ) needs to be chosen as the characteristic length ( $L_c$ ), since that length scale mostly determines the circulating flow patterns. Numerical results have shown that when the velocity ratio is less than 1, the flow circulation is controlled by the buoyancy force ( $F_b$ ), while it is dominated by the electric force ( $F_e$ ) when the velocity ratio is more than 10. Conditions that led to the

velocity ratios between 1 and 10 exhibit features dominated by both effects. It is important to recognize that both  $U_e$  and  $U_b$  are *proportional* to certain physical terms, while the proportionality constant for each term is unknown. For this reason, the transition between  $F_b$  and  $F_e$  dominant regions happens when the velocity ratio is between 1 and 10. Numerical simulations performed in varying size domains have shown that under certain conditions, the maximum flow velocity drops below  $1 \mu\text{m/s}$ , for which, diffusive transport dominates over fluid convection for most practical applications in water. **Figure 4.4** is a *phase-diagram* that distinguishes the regions of buoyancy-driven versus electrothermal-driven flows as a function of the channel height,  $H$ , and the applied electric potential,  $\phi_0$ . The transition region for  $1 < U_e/U_b < 10$  is also shown in the map, along with the regions with fluid velocities less than  $1 \mu\text{m/s}$ . It is important to indicate that the velocity ratio has no dependency on the fluid conductivity. However, both  $U_e$  and  $U_b$  linearly depend on the fluid conductivity because Joule heating is the reason for temperature changes in the system that induces both flow patterns. Joule heating is more dominant in high conductivity buffers; as a result, the diagram shows different cutoff regions for reasonable fluid flow at various conductivities. According to this diagram, higher applied potentials are required in lower conductivities to generate a reasonable flow field ( $U > 1 \mu\text{m/s}$ ) in the microchannel.

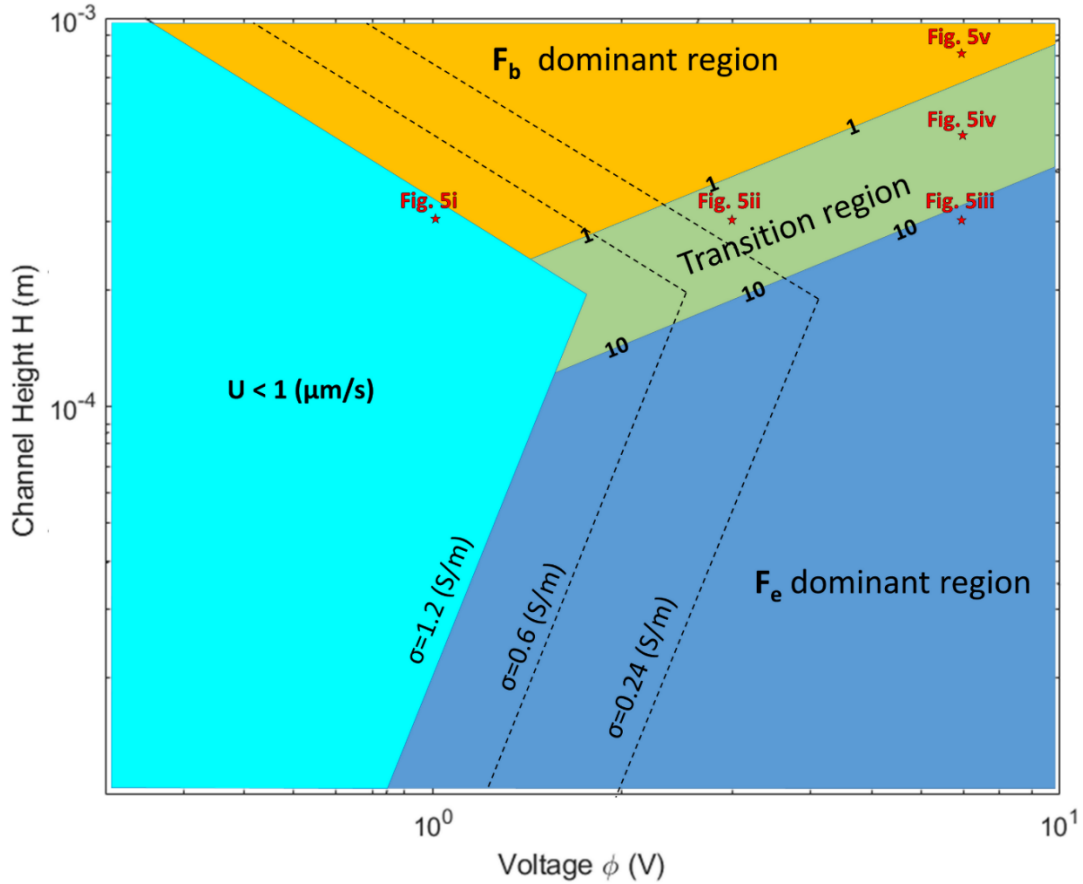


**Figure 4.4.** The phase-diagram for dominance of  $F_e$  versus  $F_b$  in the microchannel is based on their induced velocity ratio. This ratio was found for channel heights ( $H$ ) varying from  $10\ \mu\text{m}$  to  $1\ \text{mm}$  and applied electric potentials ( $\phi$ ) varying from  $0.3\ V_{pp}$  to  $10\ V_{pp}$ . The minimum velocity ( $1\ \mu\text{m/s}$ ) line for three different buffer conductivities of  $\sigma = 1.2\ \text{S/m}$ ,  $\sigma = 0.6\ \text{S/m}$ , and  $\sigma = 0.24\ \text{S/m}$  are also shown.

In order to demonstrate the effects of  $F_e$  and  $F_b$  separately and together in a microchannel system, we present in **Figure 4.5** the streamlines, velocity vectors, and speed contours in  $300\ \mu\text{m}$  height channel at applied electric potentials of  $\phi=1\ V_{pp}$  and  $\phi=7\ V_{pp}$ . The buffer was assumed to be  $0.1\ \text{M KCl}$ , leading to  $\sigma=1.2\ \text{S/m}$ . Comparisons between **Figure 4.5A** and **Figure 4.5B** show that the electrothermal ( $F_e$ ) and buoyancy ( $F_b$ ) driven flows create qualitatively similar flow patterns, where the velocity magnitudes increase with increased electric potential, as indicated by the contour map values in each figure. However,

combining both effects ( $F_e + F_b$ ) results in the flow patterns shown at the bottom row of **Figure 4.5**. At  $\varphi=1 V_{pp}$ , buoyancy driven flow wins over the ETF, but the resulting maximum velocity is below  $1 \mu\text{m/s}$ . However, ETF wins over the buoyancy driven flow at  $\varphi=7 V_{pp}$ . Although the buoyancy driven flow is approximately 23% of ETF in magnitude, it modifies the secondary vortices above the electrodes, while the ETF dominates over the region immediately above the electrode separation region. Interestingly, the ETF and the resulting mixed ( $F_e + F_b$ ) flow both exhibit downward flow towards the electrodes immediately above the electrode gap region. Accurate prediction of such flow patterns is essential if the ETF is used for sample convection and mixing purposes. It is important to indicate that the results in this case have a velocity ratio of approximately  $U_e/U_b = 12.4$  which is in the ETF region shown in **Fig 4.4**.

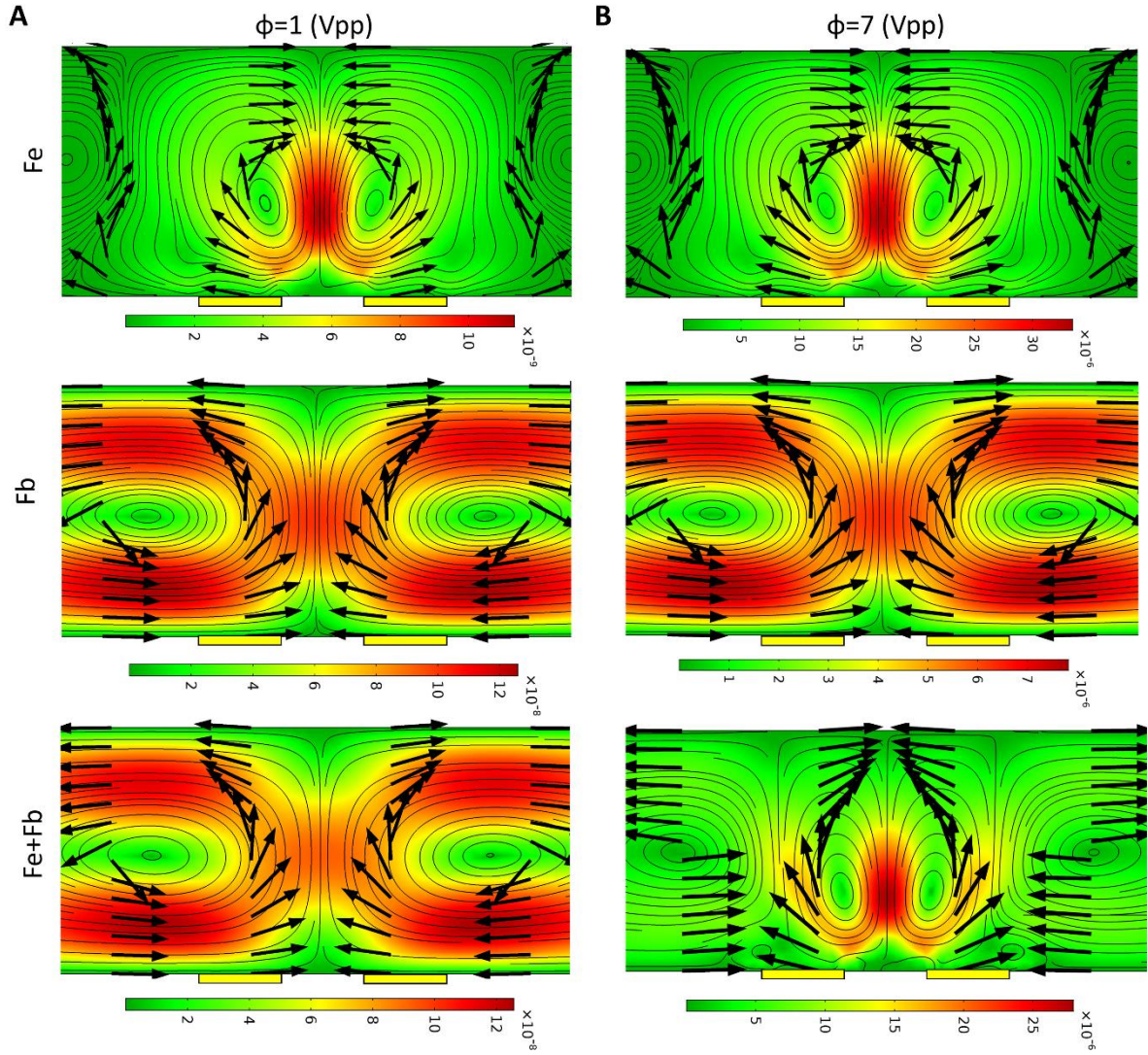


**Figure 4.5.** Streamlines, velocity vectors, and the speed contours in a 300  $\mu\text{m}$  height channel under the effects of  $F_e$ ,  $F_b$ , or  $F_e+F_b$  at **A)**  $\varphi=1$   $V_{pp}$  and **B)**  $\varphi=7$   $V_{pp}$  electric potential.

According to **Equation 4.11**, the ionic conductivity is not a function of the velocity ratio. Therefore, it should not affect the resulting flow patterns, but it should only change the velocity magnitudes in the channel. In order to illustrate this independency, different cases were simulated in two different buffer conductivities at applied electric potentials of  $\varphi = 1$

$V_{pp}$  and  $\varphi = 7 V_{pp}$ . **Figure 4.6A** and **Figure 4.6B** show the cases with buffer conductivities of  $\sigma=1.2$  S/m and  $\sigma = 0.24$  S/m at  $\varphi = 1 V_{pp}$ , while **Figure 4.6C** and **Figure 4.6D** show the cases with buffer conductivities of  $\sigma = 1.2$  S/m and  $\sigma = 0.24$  S/m at  $\varphi=7 V_{pp}$ . These figures illustrate that although the velocity magnitudes are different for these cases, the qualitative flow field remains the same. It is important to notice that the flow patterns for  $\varphi=1 V_{pp}$  show the dominance of buoyancy driven flow, while ETF dominates for  $\varphi=7 V_{pp}$  at both conductivities. **Figure 4.6E** and **Figure 4.6F** show the variation of the maximum temperature and velocity in the microchannel as a function of the applied potential for three different ionic conductivities. According to these figures, an increase in the electric conductivity or applied potential leads to higher induced temperature, thereby strengthening the generated vortices around the electrodes.

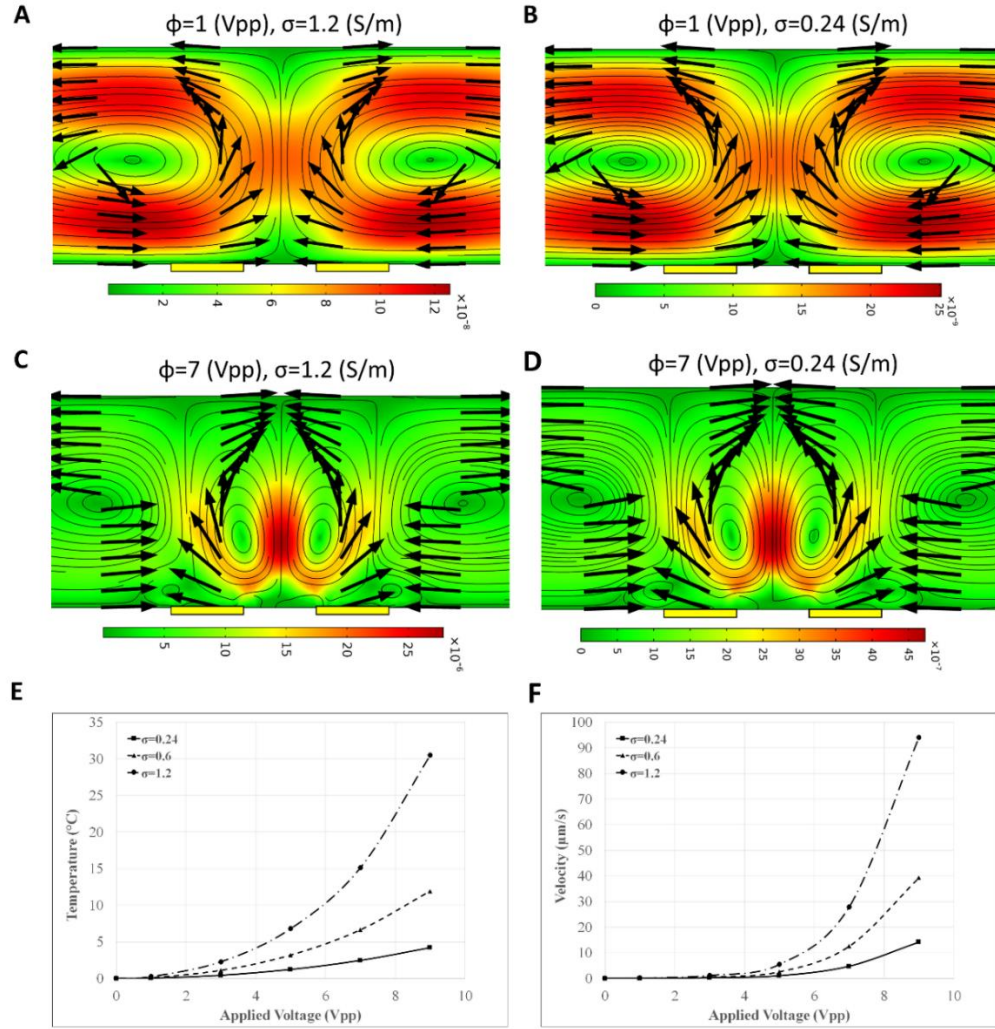


**Figure 4.6.** Velocity vectors, speed contours and the streamlines for **A)**  $\phi=1$  V<sub>pp</sub>,  $\sigma=1.2$  S/m, **B)**  $\phi=1$  V<sub>pp</sub>,  $\sigma=0.24$  S/m, **C)**  $\phi=7$  V<sub>pp</sub>,  $\sigma=1.2$  S/m, **D)**  $\phi=7$  V<sub>pp</sub>,  $\sigma=0.24$  S/m. **E)** Maximum induced temperature in the channel for three different buffer conductivities. **F)** Maximum induced velocity in the channel for three different buffer conductivities.

In order to further validate the diagram presented in **Figure 4.4**, we investigated the resulting flow in microchannels with heights varying from 300  $\mu\text{m}$  to 800  $\mu\text{m}$  under 1 V<sub>pp</sub> to 7 V<sub>pp</sub> excitations. The resulting streamlines, velocity field, and speed contours are shown in **Figure 4.7**. Simulations were conducted for 0.1M KCl at  $\sigma = 1.2$  S/m. Column A shows the transition from mostly buoyancy driven flow to ETF through increased applied

potential through figures **Figure 4.7i** to **Figure 4.7iii**. Resulting circulation patterns show the emergence of ETF at  $3 V_{pp}$ , which becomes locally dominant above the electrode separation region, while a primary circulation pattern from the buoyancy driven flow prevails above the electrodes. Column B, on the other hand, shows the presence of the ETF above the electrode gap region while the transport in most of the domain is dominated by buoyancy driven flow with increased channel height at fixed applied potential through figures **Figure 4.7iii** to **Figure 4.7v**.

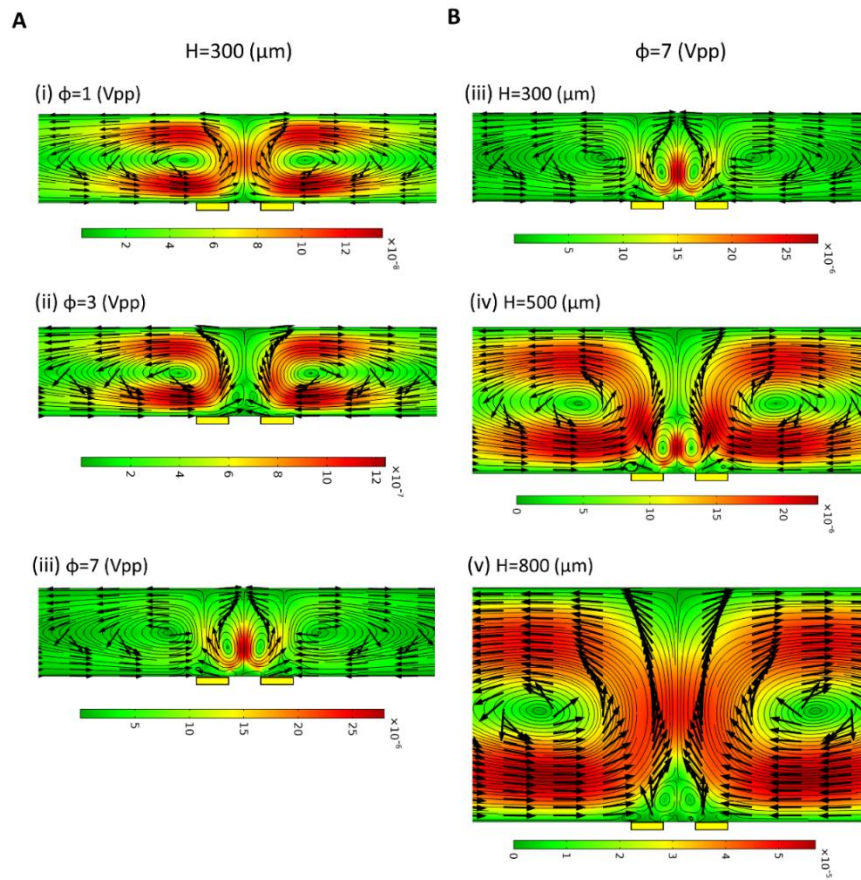


**Figure 4.7.** Effects of  $H$  and  $\phi_0$  on the streamlines, velocity vectors and speed contours. Column A shows the effects of increasing applied potential at constant channel height  $H=300 \mu\text{m}$ . Column B shows the effects of increasing channel height at constant applied electric potential of  $\phi=7 V_{pp}$ .

**Figure 4.8** shows the flow patterns in microchannel heights varying from 800  $\mu\text{m}$  to 50  $\mu\text{m}$  at 7  $V_{pp}$  applied potential. It is important to indicate that  $U_e$  is suppressed by the upper channel wall at small channel heights, and there is almost no significant flow around the electrode for channel heights less than 50  $\mu\text{m}$ . An increase in the channel height results in two induced downward vortices arising from the electric field up to 300  $\mu\text{m}$ . Then, the buoyancy driven flow dominates with the exception of a small ETF flow region immediately on top of the electrode gap.

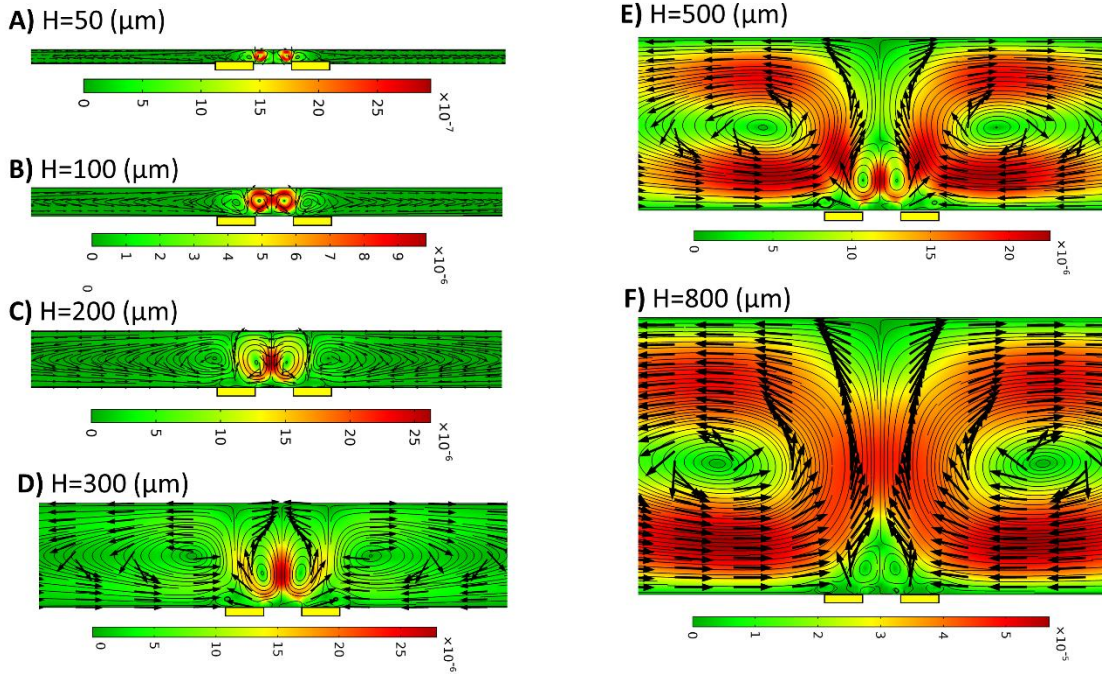


**Figure 4.8.** Velocity vectors, speed contours and the streamlines at  $\phi=7 V_{pp}$  and for different channel heights of **A)**  $H=50 \mu\text{m}$ , **B)**  $H=100 \mu\text{m}$ , **C)**  $H=200 \mu\text{m}$ , **D)**  $H=300 \mu\text{m}$ , **E)**  $H=500 \mu\text{m}$ , **F)**  $H=800 \mu\text{m}$ .

Although the numerical simulations show convection within the fluid due to the combined effect of  $F_e$  and  $F_b$ , the heat transfer mechanism in the system needs to be characterized according to the Rayleigh number ( $Ra$ ), which characterize the importance of the buoyancy driven flow, and defined as:

$$Ra = \frac{\rho_m g \beta \Delta T L_c^3}{\alpha \mu} \quad (4.12)$$

When the  $Ra$  number is below the critical value of 1708, conduction heat transfer dominates for fluid between parallel plates [55]. However, when the  $Ra$  number exceeds this critical value, convection heat transfer becomes significant and impacts the temperature distribution in the fluid. According to the fluid properties and geometric dimensions, the  $Ra$  number for most microfluidic devices operating with ETF is less than the critical value. Therefore, heat transfer in these systems is dominated by heat conduction. However, the fluid density varies inside the device due to the temperature distribution. Therefore, fluid with low density moves upward and gets away from the hot region. This motion induces a convective flow in the channel [56]. However, this convective flow affects heat transfer in the channel only at  $Ra$  numbers above the critical value. **Figure 4.9** shows temperature contours in the fluid and glass regions for microchannel heights varying from 800  $\mu\text{m}$  to 2500  $\mu\text{m}$ . Column A shows the results for conduction heat transfer by solving **Equation 2.12**, while Column B shows temperature contours for both conduction and convection considering **Equation 2.10**. The latter cases have  $Ra$  numbers of 182, 1200, 2850 and 5560 for 800  $\mu\text{m}$ , 1500  $\mu\text{m}$ , 2000  $\mu\text{m}$  and 2500  $\mu\text{m}$  height channels, respectively. The dominance of heat conduction is apparent for the  $H < 1500 \mu\text{m}$  cases, while convective heat transfer effects increase for Rayleigh numbers above the critical value and start affecting the temperature distribution in the channel.

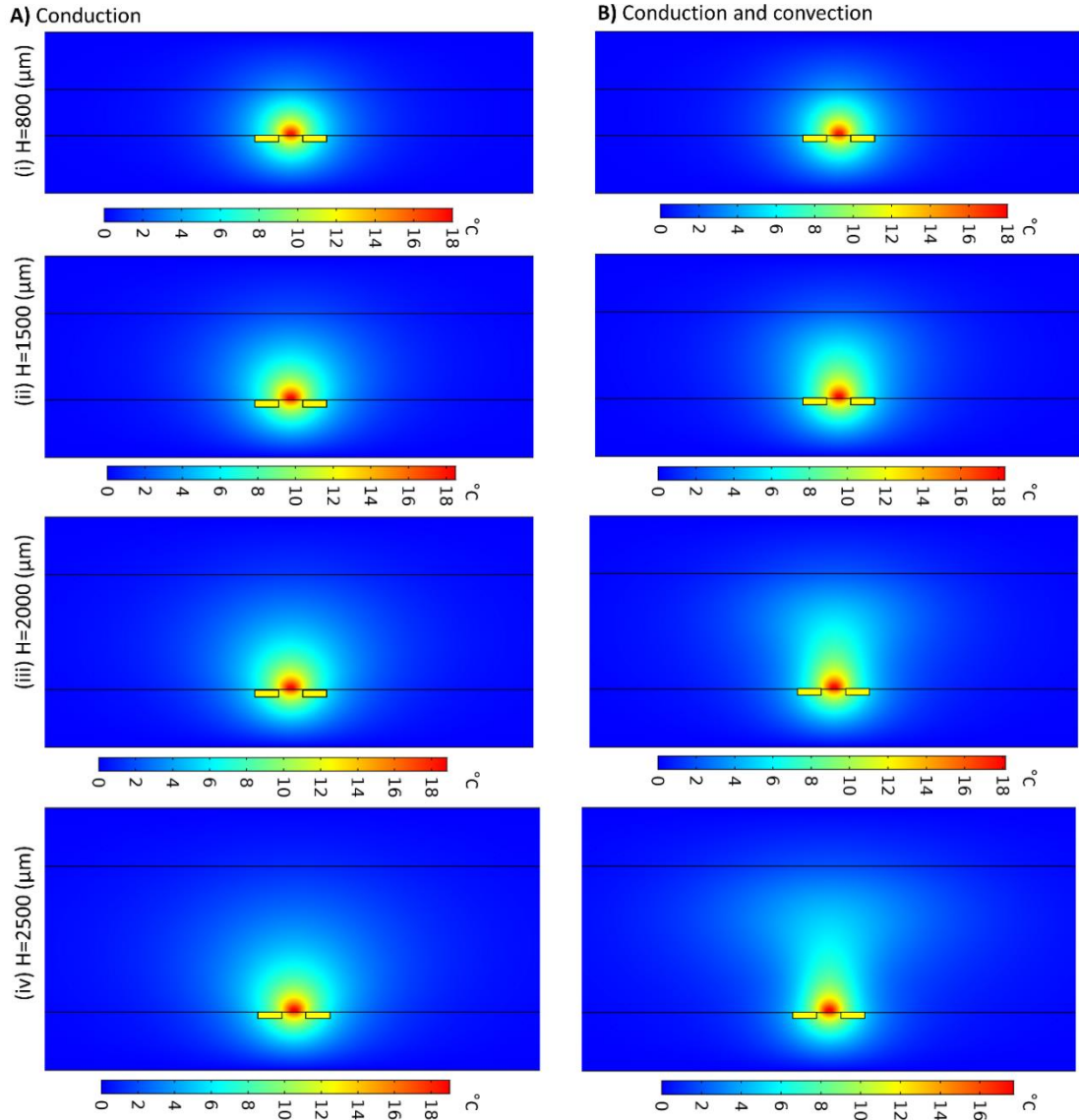


**Figure 4.9.** Temperature contours around the pair of electrodes within a microchannel with different heights for **A)** conduction only, and **B)** a combination of conduction and convection heat transfer mechanisms. The Rayleigh numbers are 182, 1200, 2850, and 5560 for column B, i to iv, respectively. The applied electric potential is  $\phi=7 V_{pp}$ .

In order to validate the numerical results, we performed microparticle image velocimetry measurements in a  $H=300 \mu\text{m}$  microchannel with two sputtered gold electrodes. Each electrode was  $100 \mu\text{m}$  wide, with a gap of  $d=100 \mu\text{m}$  separating them. **Figure 4.10A** shows the region of interest (ROI) within the electrode pair. Since the electrodes are opaque and

we cannot image particles over the electrodes, we specifically selected the region shown in the box on the left figure. The right figure shows velocity vectors in the horizontal plane and the corresponding velocity contours measured approximately 70  $\mu\text{m}$  above the planar electrodes under 7  $V_{\text{pp}}$  electric potential. Strong flow towards the electrode separation gap region is observed. The numerical results shown in **Figure 4.7iii** show a similar flow pattern. Both simulation and the PIV results show an increase in the fluid velocity towards the electrodes, where  $F_e$  and  $F_b$  are dominant due to the increased electric field and temperature rise. **Figure 4.10B** shows the velocity magnitude in the y-direction in the ROI, and compares the experimental and simulation results. This figure demonstrates that velocity is higher near the electrode and decreases away from the electrodes. Error bars in the experiments were obtained by calculating the standard deviation in this one-dimensional velocity field in the lateral direction. The pointwise agreement between the simulation and experiments is remarkable. **Figure 4.10C** shows the effect of electric potential on the average velocity in the ROI. This figure also compares the numerical simulations with experimental data. **Figure 4.10C** illustrates that increased applied potential enhances the ROI's velocity magnitude. This is mainly because both  $F_e$  and  $F_b$  depend on the applied voltage, which enhances the flow field in the microchannel.

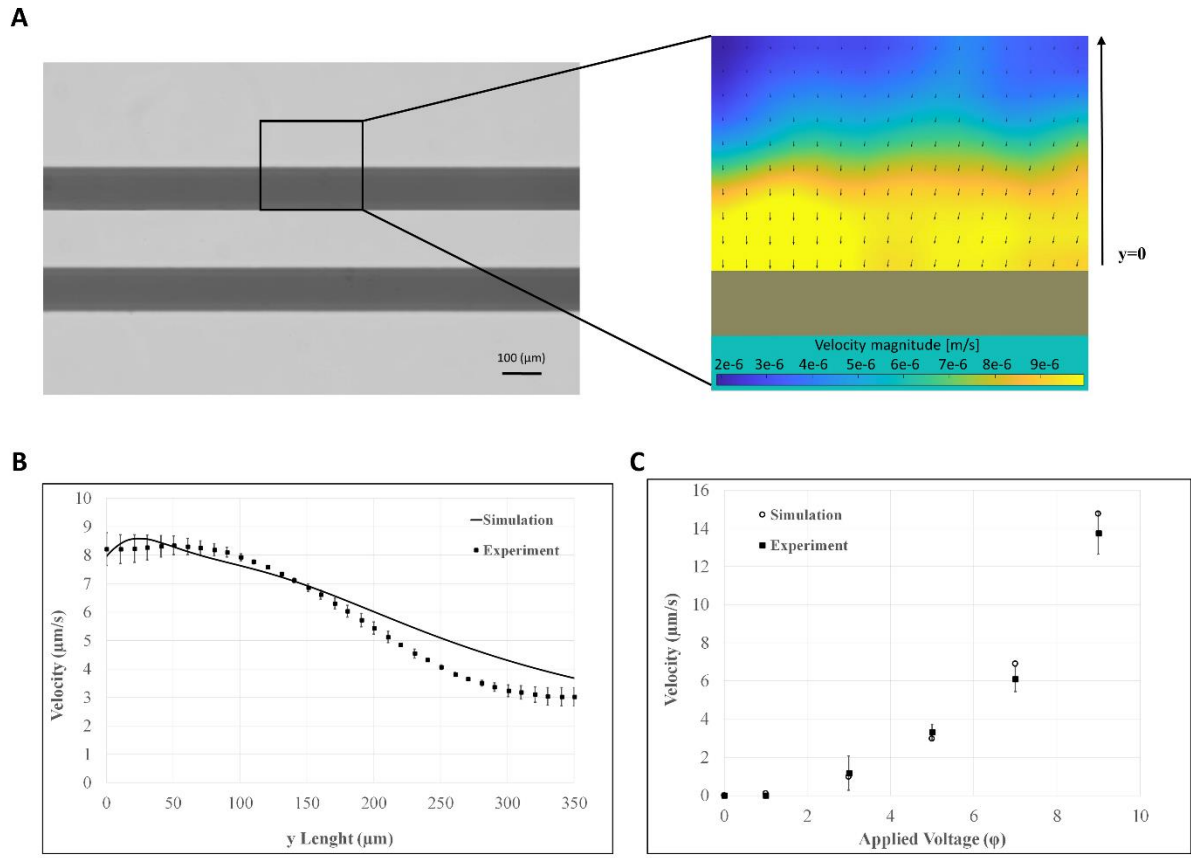


**Figure 4.10.** Experimental results for flow field at an ROI  $70\ \mu\text{m}$  above the electrodes. **A)** PIV result for the velocity field in the ROI at  $\phi_0=7\ V_{pp}$  from the bottom view of the electrodes, **B)** Velocity magnitude in the  $y$ -direction compared with the simulation result at  $\phi_0=7\ V_{pp}$ , **C)** Average velocity magnitudes in the ROI compared with the numerical simulation results at different applied voltages.

### 4.3. Conclusion

Joule heating-induced transport in microfluidic devices occurs mostly in high-conductivity media like physiological buffers, and results in co-occurring buoyancy-driven and electrothermal flows. When the electrodes are placed at the bottom of the microchannel, competing ACET and buoyancy driven flows are observed. Current work analyzed this configuration to determine the relative importance of each phenomenon. Proper

nondimensionalization of the governing equations led to a new dimensionless parameter, defined as the ratio of the velocities obtained from electrothermal versus buoyancy driven flows. Using a range of device dimensions and applied electric potentials, and by considering the ionic conductivity of the medium, a *phase diagram* indicating buoyancy versus electrothermal effects are developed. The phase diagram was verified using parametric numerical studies and validated using micro-PIV experiments. At small channel dimensions and high electric potentials ACET flow dominates, while buoyancy driven flow takes over at larger channel heights. Irrespective of the controlling phenomena, the local flow field shows regions of the dominance of the other. For example, flow immediately above the electrodes is mostly influenced by ACET, while the rest of the domain may exhibit buoyancy driven flow. Understanding of the resulting flow patterns are crucial for utilizing Joule heating for sample convection and mixing in Lab-on-a-Chip applications. While vortical structures and flow circulation regions exist, heat transfer in the system is mostly dominated by heat conduction for as long as the Rayleigh number is lower than the critical value.

## Chapter 5

### EFFECT OF GOLD NANOSTRUCTURED ELECTRODES ON BIOSENSING EFFICIENCY

Detection of antibody-antigen interaction in an electrochemical immunoassay biosensor in a high conductive buffer can be challenging due to the electropolarization (EP) effect. The EP effect usually occurs at the sub-MHz frequency range in high-conductive media. It stems from ion accumulation at the electrode/electrolyte interface, which creates a large interfacial capacitance. Electrodeposition of gold nanostructure on planar gold electrodes is one of the EP reduction techniques. In the present chapter, we used this method to reduce EP and characterized the interaction between bovine IgG and anti-bovine IgG in a highly conductive buffer. The detection response was indicated by recording the impedance of the devices in real time during antibody–antigen interaction on the electrode surface. In order to find the optimum detection frequency of the sensor, the impedance of the microfluidics device was measured in a range of frequencies varying from 100 Hz to 10 MHz. This chapter is organized as follows. Fabrication methods, experimental material, and procedures, such as buffer preparation, dilution, and electrode immobilization procedures, are explained in the materials and methods section. Then, the detection results from the experiments are discussed.

## 5.1. Materials and method

### 5.1.1. Device fabrication and experimental setup

To fabricate the devices used in experiments, standard photolithography was employed. The first step involved thoroughly cleaning the glass substrate. To accomplish this, 25 mm × 25mm × 1mm glass slides were subjected to a three-step washing process using 1M KOH, acetone, isopropyl alcohol, and DI water in an ultrasonic bath (FB11201, Fisher Scientific, Waltham, MA, USA) in 25 °C and 37 kHz operation condition. After each step, the glass slides were rinsed with DI water from the Millipore Alpha-Q water system (Bedford, MA, USA). The glass slides were dried using nitrogen and then placed in an oven for complete drying (20GC Lab Oven, Quinvy Lab Inc.) at 150 °C. After 20 minutes in the oven, the glass slides were cooled to room temperature, and a positive photoresist (S1813) was applied to the surface using a spin coater. A multi-stage rotation speed was chosen to create a smooth layer of photoresist on the glass surface (1000 rpm and 4000 rpm for 10 (s) and 30 (s), respectively, with 300 rpm/s acceleration/deceleration stages). The coated glass substrates were then soft-baked for 1 minute at 115°C on a hot plate, followed by preparation for UV light exposure. 110 (mJ/cm<sup>2</sup>) The substrate was then exposed to UV light using a mask aligner, with a designed transparency mask covering the substrate (Karl Suss, MJB3). After UV treatment, the substrates were immersed in a developer solution (MF-26A) to remove the areas exposed to UV light. Following that, a 3 nm chromium layer and a 22 nm gold layer were deposited on the surface of the glass slides using a sputter coater (EMS300TD, Emitech). The unexposed photoresist and metal layers were then removed from the surface by submerging the coated glass slides in a PG remover solution at 80°C. Afterwards, copper tape was attached to the electrode tips for

the application of an electric potential. A three-electrode potentiostat/galvanostat system (EZstatPro, Novant) was used to deposit the gold nanostructure on the electrodes. The gold surface was immersed into the electrolyte (0.5 mg/ml Sodium Tetrachloroaurate (III) ( $\text{AuCl}_4\text{Na}_2\text{H}_2\text{O}$ ) solution (Sigma Aldrich)) as the working. The voltage on the surface of the working electrode is controlled with Ag/AgCl reference electrode (MF-2052, BASI). The charge transfer reaction and deposition of the film on the surface of the electrode occurred due to the electric current flowing between the working electrode and counter electrode, which were connected to a three-electrode potentiostat system.

To create the microchamber, a double-sided tape with a thickness of 50  $\mu\text{m}$  and dimensions of 15 mm  $\times$  2 mm was cut using a craft cutter (Silver Bullet). The height of the microchamber was determined by the tape layers placed between the electrode substrate and the sliding glass on the top and bottom. **Figure 5.1A** shows the interdigitated electrodes with 200  $\mu\text{m}$  width and 200  $\mu\text{m}$  spacing that was fabricated through this procedure. The impedance measurement was performed using an impedance analyzer (HP Agilent 4194A). The microchip copper wires were connected to the analyzer, which applied the desired electric potential at a specified frequency and simultaneously recorded the impedance. To ensure the reliability of the voltage and frequency applied by the impedance analyzer, the oscilloscope (TDS 2014B by Tektronix) was employed to measure these values before the experiments. **Figure 5.1B** illustrates the experimental setup used for detection.

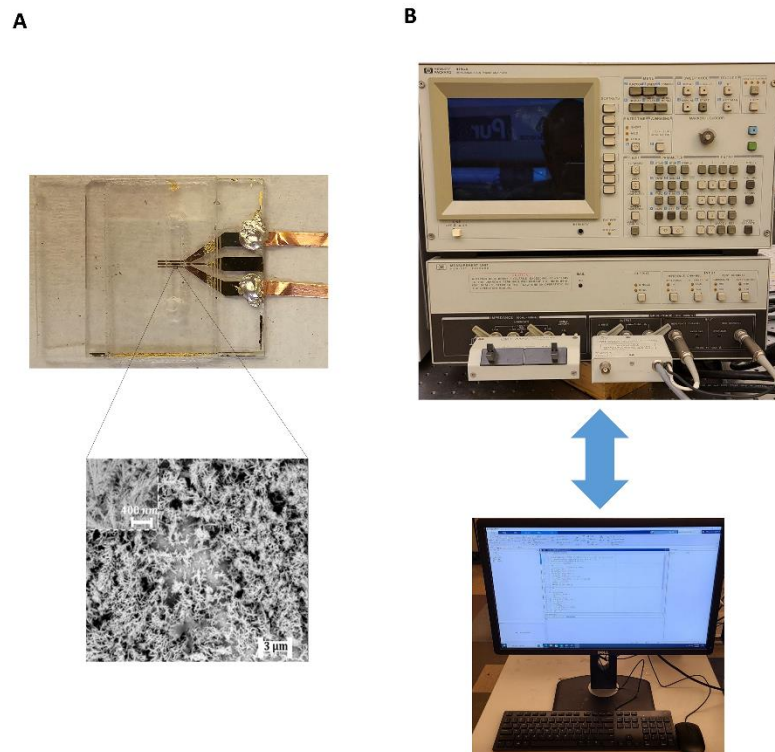


**Figure 5.1.** A) Fabricated device using the photolithography method and the gold nanostructure on the electrode surface, B) Experimental setup.

#### 5.1.2. Buffer preparation and immobilization procedure

A 1x PBS solution of conductivity 1.6 S/m was prepared by diluting a 10x PBS stock solution (from Fisher Scientific) with DI water at a ratio of 1:10. The limit of detection (LOD) of the sensor was determined by studying the binding of anti-bovine IgG (H+L) antibody (from Jackson ImmunoResearch Laboratories Inc.) to whole bovine IgG molecules (from Jackson ImmunoResearch Laboratories Inc.). The bovine IgG was diluted with 1xPBS to a concentration of 10 μg/mL for immobilization on the electrode surface. The chemical cross-linking technique was used to immobilize proteins on the gold electrode surface [57].

The most commonly used chemical cross-linker for linking gold and protein is dithiobis(succinimidyl propionate) (DSP, Product No. 22585). DSP forms a highly stable linkage with the gold surface. It chemisorbs quickly to the gold through its disulfide linkage, and its active NHS groups on either end are reactive with proteins. The concentration of DSP should be 4 mg per mL of DMSO to ensure adequate coverage of the gold surface. Then, the covered gold electrode, with the DSP solution, should be incubated at room temperature for 30 minutes. After incubation, the electrode was rinsed with DMSO and DI water. This activates the gold foil with NHS groups. Afterward, the electrode surface was completely covered with the bovine IgG whole molecules (1 mg/ml) diluted with PBS solution. If the protein immobilization process is delayed, the NHS reactive groups will hydrolyze, causing a significant decrease in protein coupling. Then, the loaded device was kept inside a humidity chamber at 4°C for 4 hours to functionalize the electrodes. Extending the incubation time will not negatively impact conjugation efficiency, but there will not be a significant improvement in conjugation after the first 1-2 hours. Afterward, the electrode was rinsed using 1xPBS to wash away any by-products from the cross-linking process and unbound proteins. Then, the chip was ready to detect anti-bovine IgG.

The anti-bovine IgG was diluted with PBS to concentrations of 100 ng/mL for detection. The chamber was filled with the diluted anti-bovine IgG in desired concentrations, and impedance changes were measured and recorded continuously while the AC voltage was applied to the electrodes.

## 5.2. Results and discussions

The gold nanostructure deposition method on the electrodes has been widely used to characterize the interfacial impedance at the electrode/electrolyte surface for gold planar electrodes (GPE) and gold nanostructured electrodes (GNE) in high conductive buffer [58]. Also, recently we proposed a microfluidic device for cell screening in high-conductivity physiological media with the GNEs in sub-MHz frequencies, which showed better sensitivity compared to the GPEs at the same frequency range [37]. Based on these experiences, we studied the bovine IgG and anti-bovine IgG interaction on GNE and GPE. The electrode pattern consists of three interdigitated electrodes with 200  $\mu\text{m}$  width and 200  $\mu\text{m}$  spacing. 50 mV was applied to the electrodes in a frequency range from 100 Hz to 10 MHz [26]. To find the effective detection frequency for GPE and GNE, impedance changes for the anti-bovine IgG with 100 ng/ml concentration diluted with 1xPBS were obtained for the frequency range. **Figure 5.2** shows the impedance magnitude and phase angle for the GPE and GNE. **Figure 5.2A** shows a reduction in impedance magnitude, and **Figure 5.2B** shows that phase angle  $\alpha$  has a shift toward less negative values after the deposition of gold nanostructure on the planar electrodes. The phase angle behavior at low AC frequencies shows that the electric double layer (EDL) for the GPE is more capacitive, while it behaves mixed capacitive and resistive for the GNE case. This type of EP reduction using the electrodeposition technique was also previously shown in the literature [37, 58].

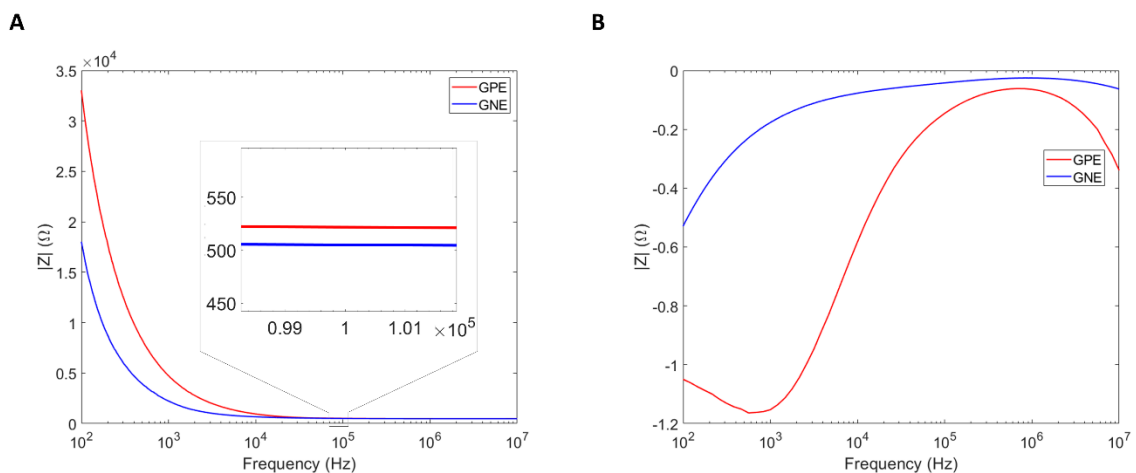


**Figure 5.2.** Comparing **A)** impedance magnitude and **B)** phase angle for GPE and GNE

**Figure 5.3A** shows the impedance magnitude of the GPE as a function of frequency before immobilization, after immobilization, and 30 min after the anti-bovine IgG was applied to the electrode surface, and **Figure 5.3B** shows the phase angle. According to these two figures, after antibody immobilization, at low frequency, the impedance magnitude increases, and the phase angle gets more capacitive, while at high frequencies, the change in these two parameters is insignificant. This capacitive behavior is due to the thin layer of immobilized antibodies on the electrode, which acts like an insulating layer.

**Figure 5.3C** shows the impedance magnitude of the GNE as a function of frequency before immobilization, after immobilization, and 30 min after the antibody-antigen interaction, and **Figure 5.3D** shows the phase angle. According to these two figures, the GNE impedance magnitude and phase angle change at the applied frequency spectra is lower. Although the gold nanostructure reduces the EP effect, because of this structure's porous nature and the pattern's disorganized growth, the immobilized antibodies trapped inside the pores may reduce the overall number of interaction sites on the electrode surface.

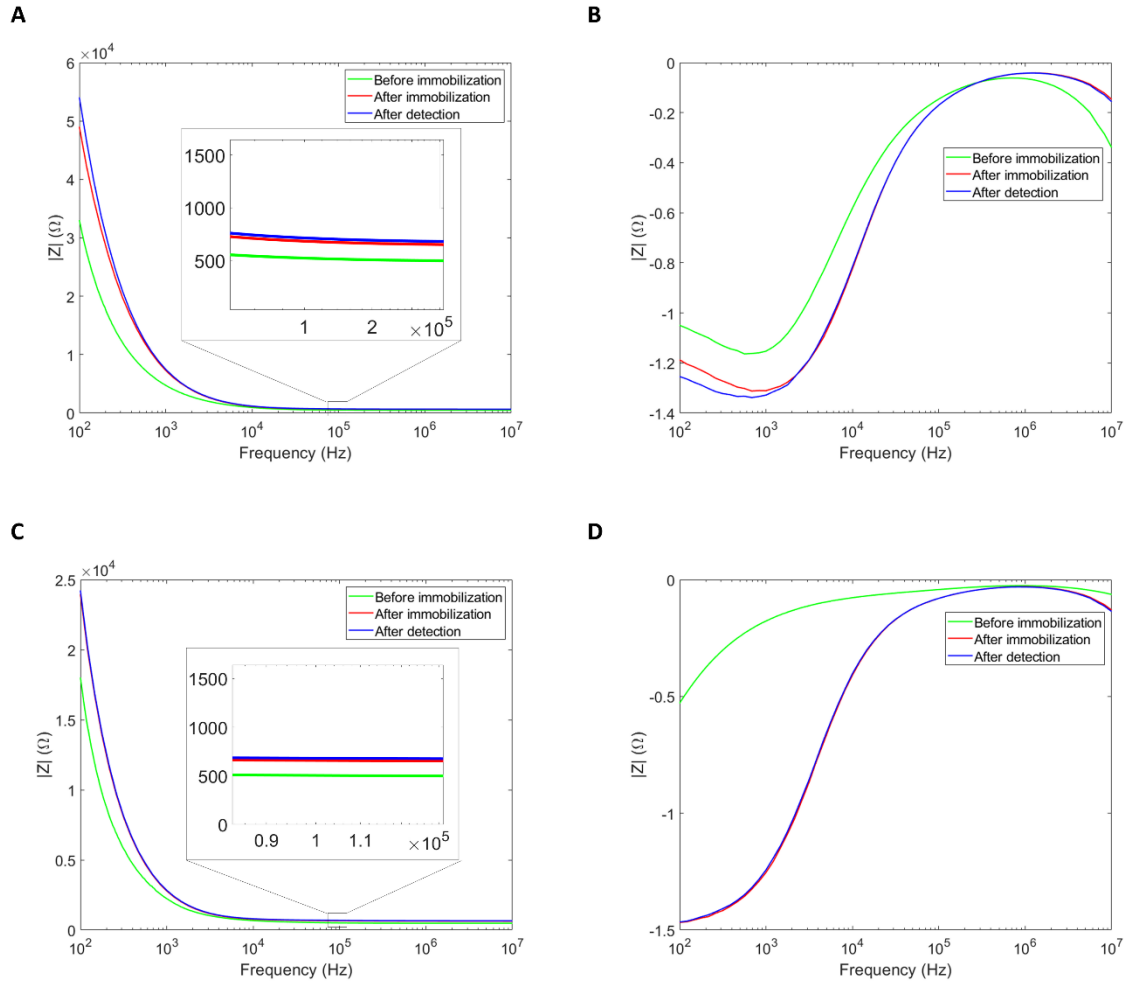


**Figure 5.3.** Impedance spectra of the electrodes in 1xPBS, for electrodes with 100 ng/ml antigen immobilized on the electrode surface, and 30 min after antibody-antigen interactions. **A)** GPE Impedance magnitudes, **B)** GPE phase angle, **C)** GNE Impedance magnitudes, **D)** GNE phase angle.

**Figure 5.4** compares the impedance magnitude change for GPE and GNE in the frequency range. **Figure 5.4A** shows the impedance change of the GPE as a function of frequency 30 min after the anti-bovine IgG was applied to the chamber. **Figure 5.4B** shows the impedance changes after 30 min for GNE. According to this figure, impedance change due to antibody capture drops dramatically after the deposition of gold nanostructures on the electrode.

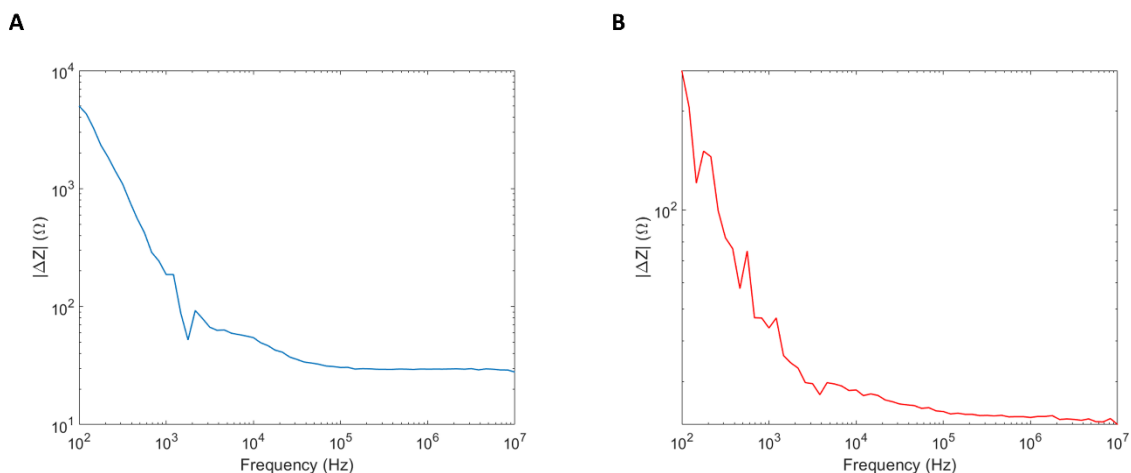


**Figure 5.4.** Impedance changes 30 minutes after antibody-antigen interaction for 100 ng/ml antigen concentrations diluted in 1xPBS applied on the immobilized electrode surface for **A)** GPE and **B)** GNE.

In order to have a more detailed comparison of these results, the percent of normalized impedance changes with the initial impedance at each frequency is shown in **Figure 5.5**. Here  $\Delta|Z|/|Z_0|$  is defined as the impedance change 30 minutes after antibody-antigen interaction at a frequency divided by the impedance magnitude at that frequency at  $t=0$ . This figure demonstrates that, for GPE, normalized impedance change reduced dramatically at the low frequency range from 100 Hz to 1000 Hz. Then, it increased to 5% and remained nearly constant for the rest of the frequency domain. However, for the GNE, the normalized impedance change starts from almost 1% at 100 Hz, and increases to 3.5% at 10 kHz. Then it remains almost the same by increasing the frequency. Comparing these two figures, we realize that the electrodeposited gold nanostructured electrodes (GNE) impedes detection at low frequencies and does not result in enhanced detection at high frequencies either. This is probably due to the porous nature of the GNE, which increases

the electrode surface area and reduces the EP effect, but it does not allow antibody-antigen interactions in a porous matrix.

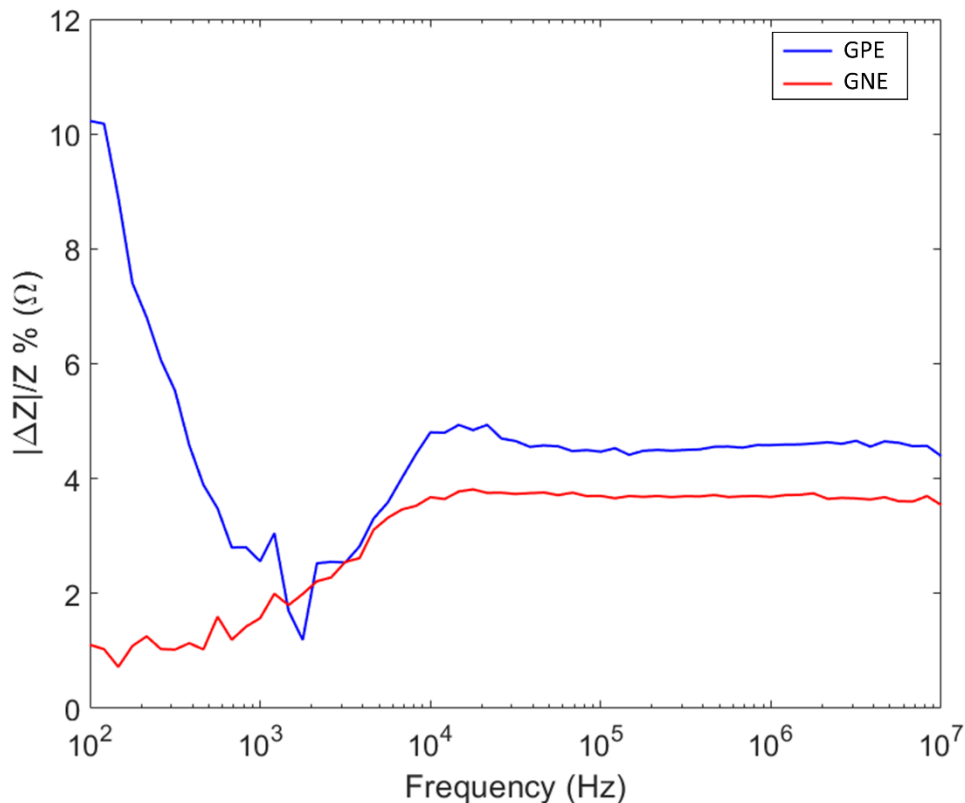


**Figure 5.5.** Comparing  $|\Delta Z|/|Z|$  for GPE and GNE

### 5.3. Conclusion

The EP effect occurs mostly in high-conductivity media like physiological buffers and accumulates ions at the electrode/electrolyte interface, creating a large interfacial capacitance. When the electrode/electrolyte interfacial area increases, it reduces EP. The current chapter analyzed the increase in the surface area of the electrodes using electrodeposition of gold nanostructure on planar electrodes to enhance detection and

reduce EP effect in the low frequency range. In order to characterize detection, bovine IgG and anti-bovine IgG interaction on an interdigitated electrode with 200  $\mu\text{m}$  width and the gap was studied in a frequency range from 100 Hz to 10 MHz. The results demonstrated for GPE that there is a greater impedance change than the GNE, and the EP effect (charge accumulation) is reduced after the deposition of gold nanostructure. However, the nanostructure reduces the overall detection when the ( $|\Delta Z|/|Z_0|$  %) for GPE and GNE are compared. This is mainly due to the porous nature of this structure, which may trap the antibody inside them and requires antibody-antigen interaction through a porous matrix during the detection phase.

## Chapter 6

### SUMMARY AND FUTURE RESEARCH

The present dissertation investigates transport mechanisms in electrochemical biosensors for characterizing SARS-CoV-2 neutralizing antibody (NAb) in a buffer. In order to extend the application to detection in the high conductive buffers, two parameters, including Joule-heating based transport and electrode polarization (EP) effect reduction, are studied. This chapter summarizes the key findings from the study, and directions for future research are proposed.

#### 6.1 Summary of the current work

Electrochemical immunoassay biosensors have been widely studied due to their accurate, fast, quantifiable results at a low cost. A large number of researchers claimed the ACEK transport phenomena, including ACEO, ACET, and DEP, enhance detection in affinity biosensors. In the current dissertation, these ACEK mechanisms for the most reported sensor, a modified SAW device, are studied using a scaling analysis, numerical simulations, and experiments. However, the results showed that these ACEK mechanisms have no significant effects in the sensor and most detection mechanisms are based on diffusion. Sensor limit of detection, selectivity, and specificity was investigated considering the sensor's Bovine-IgG and anti-bovine IgG interaction. Then, it was used to evaluate the SARS-CoV-2 neutralizing antibody (NAb) in a physiological buffer.

Since biological fluids like blood plasma has high electrical conductivity, Joule heating based transport would be a method of choice to enhance detection in electrochemical

immunoassay biosensors. Buoyancy-driven and alternating current electrothermal (ACET) flows are the main transport mechanisms that induce two counter directions of vortical flow around the electrodes. However, many references in the literature assumed a downward direction for the buoyancy flow that resulted in vortices with the same direction as the ACET flow. In order to clarify this type of fluid motion, the first comprehensive investigation of Joule heating induced fluid motion in microchannels around a pair of electrodes in a high conductive buffer under AC electric fields are presented in this thesis. This study reveals a competition between ACET and buoyancy driven flows, and a new non-dimensional parameter characterizes this competing effect. This new parameter was used to construct a phase diagram that enabled the prediction of the ACET and buoyancy driven flow dominance as a function of the applied electric field and channel size. The phase diagram was verified using numerical simulation and experimental techniques.

Finally, gold nanostructure deposition on planar electrodes is investigated to enhance detection by reducing the EP effect in an electrochemical immunoassay biosensor. The results demonstrated the effectiveness of the deposited gold nanostructure on the electrode for EP reduction. However, when  $(\Delta Z/Z_0 \%)$  is considered as a detection parameter, gold nanostructured electrodes did not perform as well as planar gold electrodes. This behavior was attributed to the porous structure of the GNE, where the immobilized antibodies were trapped inside the pores, and the antigen could not diffuse into the porous matrix to result in enhanced detection.

## 6.2 Future Research

The present biosensor can detect one antigen from a buffer because only one interdigitated electrode is immobilized with a specific antibody. Detecting multiple pathogens or analytes within a single sample can save time and resources compared to performing separate tests for each antigen. In future work, a microfluidic platform with multiple separated electrodes will be designed, which will be able to detect multiple antigens from a bio-sample at the same time. In order to enhance the detection time, some pair of electrodes can be placed on top of the sensing electrodes with a higher applied electric field to induce Joule-heating based transport in the device.

## References

- [1] C.B. Jackson, M. Farzan, B. Chen, H. Choe, Mechanisms of SARS-CoV-2 entry into cells, *Nature reviews Molecular cell biology*, 23 (2022) 3-20.
- [2] S.C. Taylor, B. Hurst, C.L. Charlton, A. Bailey, J.N. Kanji, M.K. McCarthy, T.E. Morrison, L. Huey, K. Annen, M.G. DomBourian, A New SARS-CoV-2 Dual-Purpose Serology Test: Highly Accurate Infection Tracing and Neutralizing Antibody Response Detection, *Journal of Clinical Microbiology*, 59 (2021) e02438-02420.
- [3] D. Cromer, M. Steain, A. Reynaldi, T.E. Schlub, A.K. Wheatley, J.A. Juno, S.J. Kent, J.A. Triccas, D.S. Khoury, M.P. Davenport, Neutralising antibody titres as predictors of protection against SARS-CoV-2 variants and the impact of boosting: a meta-analysis, *The Lancet Microbe*, (2021).
- [4] M.A. Black, G. Shen, X. Feng, W.F.G. Beltran, Y. Feng, V. Vasudevaraja, D. Allison, L.H. Lin, T. Gindin, M. Astudillo, Analytical performance of lateral flow immunoassay for SARS-CoV-2 exposure screening on venous and capillary blood samples, *Journal of immunological methods*, 489 (2021) 112909.
- [5] J. Nie, Q. Li, J. Wu, C. Zhao, H. Hao, H. Liu, L. Zhang, L. Nie, H. Qin, M. Wang, Establishment and validation of a pseudovirus neutralization assay for SARS-CoV-2, *Emerging microbes & infections*, 9 (2020) 680-686.
- [6] Food, D. Administration, USA. cPass™ SARS-CoV-2 neutralization antibody detection kit "<https://www.genscript.com/covid-19-detection-fda-eua.html>".
- [7] P. Kongsuphol, H. Jia, H.L. Cheng, Y. Gu, B.D. Shunmuganathan, M.W. Chen, S.M. Lim, S.Y. Ng, P.A. Tambyah, H. Nasir, A rapid simple point-of-care assay for the detection of SARS-CoV-2 neutralizing antibodies, *Communications medicine*, 1 (2021) 1-12.
- [8] S.M. Lim, H.L. Cheng, H. Jia, P. Kongsuphol, B. D/O Shunmuganathan, M.W. Chen, S.Y. Ng, X. Gao, S.P. Turaga, S.P. Heussler, Finger stick blood test to assess postvaccination SARS-CoV-2 neutralizing antibody response against variants, *Bioengineering & Translational Medicine*, (2022) e10293.
- [9] L. Davidi, S. Morais, L. Artzi, D. Knop, Y. Hadar, Y. Arfi, E.A. Bayer, Toward combined delignification and saccharification of wheat straw by a laccase-containing designer cellulosome, *Proceedings of the National Academy of Sciences*, 113 (2016) 10854-10859.
- [10] Y. Huang, J. Xu, J. Liu, X. Wang, B. Chen, Disease-related detection with electrochemical biosensors: a review, *Sensors*, 17 (2017) 2375.
- [11] N. Sandhyarani, Surface modification methods for electrochemical biosensors, *Electrochemical Biosensors*, Elsevier2019, pp. 45-75.

- [12] A.M. Faria, E.B. Peixoto, C.B. Adamo, A. Flacker, E. Longo, T. Mazon, Controlling parameters and characteristics of electrochemical biosensors for enhanced detection of 8-hydroxy-2'-deoxyguanosine, *Scientific reports*, 9 (2019) 1-10.
- [13] E.E. Ferapontova, Hybridization biosensors relying on electrical properties of nucleic acids, *Electroanalysis*, 29 (2017) 6-13.
- [14] J. Shi, D.M. Porterfield, Surface modification approaches for electrochemical biosensors, *Biosensors-Emerging Materials and Applications*, (2011).
- [15] S.S. Mahshid, S.E. Flynn, S. Mahshid, The potential application of electrochemical biosensors in the COVID-19 pandemic: A perspective on the rapid diagnostics of SARS-CoV-2, *Biosensors and Bioelectronics*, 176 (2021) 112905.
- [16] N.J. Ronkainen, H.B. Halsall, W.R. Heineman, Electrochemical biosensors, *Chemical Society Reviews*, 39 (2010) 1747-1763.
- [17] H. Cui, S. Li, Q. Yuan, A. Wadhwa, S. Eda, M. Chambers, R. Ashford, H. Jiang, J. Wu, An AC electrokinetic impedance immunosensor for rapid detection of tuberculosis, *Analyst*, 138 (2013) 7188-7196.
- [18] S. Li, H. Cui, Q. Yuan, J. Wu, A. Wadhwa, S. Eda, H. Jiang, AC electrokinetics-enhanced capacitive immunosensor for point-of-care serodiagnosis of infectious diseases, *Biosensors and Bioelectronics*, 51 (2014) 437-443.
- [19] S. Li, Y. Ren, H. Jiang, Convection and mass transfer enhanced rapid capacitive serum immunoassay, *Rsc Advances*, 4 (2014) 9064-9071.
- [20] C. Cheng, S. Wang, J. Wu, Y. Yu, R. Li, S. Eda, J. Chen, G. Feng, B. Lawrie, A. Hu, Bisphenol a sensors on polyimide fabricated by laser direct writing for onsite river water monitoring at attomolar concentration, *ACS applied materials & interfaces*, 8 (2016) 17784-17792.
- [21] H. Cui, C. Cheng, X. Lin, J. Wu, J. Chen, S. Eda, Q. Yuan, Rapid and sensitive detection of small biomolecule by capacitive sensing and low field AC electrothermal effect, *Sensors and Actuators B: Chemical*, 226 (2016) 245-253.
- [22] A. Mansoorifar, A. Koklu, A.C. Sabuncu, A. Beskok, Dielectrophoresis assisted loading and unloading of microwells for impedance spectroscopy, *Electrophoresis*, 38 (2017) 1466-1474.
- [23] S. Park, M. Koklu, A. BeskoK, Particle trapping in high-conductivity media with electrothermally enhanced negative dielectrophoresis, *Analytical chemistry*, 81 (2009) 2303-2310.
- [24] J. Zhang, X. Fang, Y. Mao, H. Qi, J. Wu, X. Liu, F. You, W. Zhao, Y. Chen, L. Zheng, Real-time, selective, and low-cost detection of trace level SARS-CoV-2 spike-protein for cold-chain food quarantine, *npj Science of Food*, 5 (2021) 1-6.

- [25] S. Li, Y. Jiang, S. Eda, J.J. Wu, Low-cost and desktop-fabricated biosensor for rapid and sensitive detection of circulating D-dimer biomarker, *IEEE Sensors Journal*, 19 (2018) 1245-1251.
- [26] A. Koklu, J. Giuliani, C. Monton, A. Beskok, Rapid and Sensitive Detection of Nanomolecules by an AC Electrothermal Flow Facilitated Impedance Immunosensor, *Analytical Chemistry*, 92 (2020) 7762-7769.
- [27] Q. Yuan, K. Yang, J. Wu, Optimization of planar interdigitated microelectrode array for biofluid transport by AC electrothermal effect, *Microfluidics and nanofluidics*, 16 (2014) 167-178.
- [28] F. Hong, F. Bai, P. Cheng, Numerical simulation of AC electrothermal micropump using a fully coupled model, *Microfluidics and nanofluidics*, 13 (2012) 411-420.
- [29] S. Loire, P. Kauffmann, I. Mezić, C. Meinhart, A theoretical and experimental study of ac electrothermal flows, *Journal of Physics D: Applied Physics*, 45 (2012) 185301.
- [30] S.J. Williams, Enhanced electrothermal pumping with thin film resistive heaters, *Electrophoresis*, 34 (2013) 1400-1408.
- [31] Y. Lu, Q. Ren, T. Liu, S.L. Leung, V. Gau, J.C. Liao, C.L. Chan, P.K. Wong, Long-range electrothermal fluid motion in microfluidic systems, *International Journal of Heat and Mass Transfer*, 98 (2016) 341-349.
- [32] S. Park, A. Beskok, Alternating current electrokinetic motion of colloidal particles on interdigitated microelectrodes, *Analytical Chemistry*, 80 (2008) 2832-2841.
- [33] A. Castellanos, A. Ramos, A. Gonzalez, N.G. Green, H. Morgan, Electrohydrodynamics and dielectrophoresis in microsystems: scaling laws, *Journal of Physics D: Applied Physics*, 36 (2003) 2584.
- [34] C.-H. Chu, I. Sarangadharan, A. Regmi, Y.-W. Chen, C.-P. Hsu, W.-H. Chang, G.-Y. Lee, J.-I. Chyi, C.-C. Chen, S.-C. Shiesh, Beyond the Debye length in high ionic strength solution: direct protein detection with field-effect transistors (FETs) in human serum, *Scientific reports*, 7 (2017) 1-15.
- [35] A. Koklu, A. El Helou, P.E. Raad, A. Beskok, Characterization of temperature rise in alternating current electrothermal flow using thermoreflectance method, *Analytical chemistry*, 91 (2019) 12492-12500.
- [36] A. Beskok, A. Koklu, J. Chiao, Sensor and Method for Detecting Target Molecules, Google Patents, 2021.
- [37] S. Bakhtiari, M.K. Manshadi, A. Mansoorifar, A. Beskok, A Microfluidic Dielectric Spectroscopy System for Characterization of Biological Cells in Physiological Media, *Sensors*, 22 (2022) 463.

- [38] A. Mansoorifar, A. Koklu, S. Ma, G.V. Raj, A. Beskok, Electrical impedance measurements of biological cells in response to external stimuli, *Analytical chemistry*, 90 (2018) 4320-4327.
- [39] N. Sinha, S. Mohan, C.A. Lipschultz, S.J. Smith-Gill, Differences in electrostatic properties at antibody-antigen binding sites: implications for specificity and cross-reactivity, *Biophysical journal*, 83 (2002) 2946-2968.
- [40] E. Rosenberg, *Aggregation of therapeutic antibodies in the course of downstream processing*, Imu, 2010.
- [41] D.R. Lide, *CRC handbook of chemistry and physics*, CRC press 2004.
- [42] A. Bejan, *Heat transfer: Evolution, design and performance*, John Wiley & Sons 2022.
- [43] Y.A. Cengel, S. Klein, W. Beckman, *Heat transfer: a practical approach*, WBC McGraw-Hill Boston 1998.
- [44] A. Bejan, *Convection heat transfer*, John Wiley & Sons 2013.
- [45] C.-K. Yang, J.-S. Chang, S.D. Chao, K.-C. Wu, Effects of diffusion boundary layer on reaction kinetics of immunoassay in a biosensor, *Journal of Applied Physics*, 103 (2008) 084702.
- [46] J. Yang, S.J. Petitjean, M. Koehler, Q. Zhang, A.C. Dumitru, W. Chen, S. Derclaye, S.P. Vincent, P. Soumillion, D. Alsteens, Molecular interaction and inhibition of SARS-CoV-2 binding to the ACE2 receptor, *Nature communications*, 11 (2020) 1-10.
- [47] A. Mansoorifar, A. Koklu, A. Beskok, Quantification of cell death using an impedance-based microfluidic device, *Analytical chemistry*, 91 (2019) 4140-4148.
- [48] A. Koklu, A. Mansoorifar, J. Giuliani, C. Monton, A. Beskok, Self-Similar Interfacial Impedance of Electrodes in High Conductivity Media: II. Disk Electrodes, *Analytical chemistry*, 91 (2018) 2455-2463.
- [49] A. Koklu, A. Mansoorifar, A. Beskok, Effects of electrode size and surface morphology on electrode polarization in physiological buffers, *Electrophoresis*, 40 (2019) 766-775.
- [50] W. Thielicke, R. Sonntag, *Particle Image Velocimetry for MATLAB: Accuracy and enhanced algorithms in PIVlab*, *Journal of Open Research Software*, 9 (2021).
- [51] C.D. Meinhart, S.T. Wereley, J.G. Santiago, PIV measurements of a microchannel flow, *Experiments in fluids*, 27 (1999) 414-419.
- [52] A. Prasad, R. Adrian, C. Landreth, P. Offutt, Effect of resolution on the speed and accuracy of particle image velocimetry interrogation, *Experiments in Fluids*, 13 (1992) 105-116.

- [53] Q. Ren, Investigation of pumping mechanism for non-Newtonian blood flow with AC electrothermal forces in a microchannel by hybrid boundary element method and immersed boundary-lattice Boltzmann method, *Electrophoresis*, 39 (2018) 1329-1338.
- [54] Y. Wu, Y. Ren, H. Jiang, Enhanced model-based design of a high-throughput three dimensional micromixer driven by alternating-current electrothermal flow, *Electrophoresis*, 38 (2017) 258-269.
- [55] W.M. Deen, *Analysis of transport phenomena*, (1998).
- [56] Y. Qian, S.L. Neale, J.H. Marsh, Microparticle manipulation using laser-induced thermophoresis and thermal convection flow, *Scientific Reports*, 10 (2020) 19169.
- [57] T. Scientific, Attach a protein onto a gold surface, *Tech Tip*, 2 (2008) 1-2.
- [58] A. Koklu, A.C. Sabuncu, A. Beskok, Rough gold electrodes for decreasing impedance at the electrolyte/electrode interface, *Electrochimica acta*, 205 (2016) 215-225.